# Upgrading of precast RC beam-column joints using innovative FRP/steel hybrid technique for progressive collapse prevention

Hussein M. Elsanadedy [1],*, Yousef A. Al-Salloum, Mohammed A. Alrubaidi, Tarek H. Almusallam, Nadeem A. Siddiqui, Husain Abbas

*Chair of Research and Studies in Strengthening and Rehabilitation of Structures, Dept. of Civil Engineering, College of Engineering, King Saud University, P.O. Box 800, Riyadh 11421, Saudi Arabia*

## HIGHLIGHTS

- Progressive collapse risk of strengthened precast RC beam-column joints was studied.
- Three frames (single story with two bays) were tested under middle column-loss scenario.
- Test frames included one monolithic and two precast (one control and one strengthened).
- For strengthened frame, innovative FRP/steel hybrid technique was used.
- Nonlinear 3D FE analysis with rate-dependent material models was conducted.

## ARTICLE INFO

## ABSTRACT

This study aims at investigating the efficacy of using an innovative hybrid strengthening technique composed of near-surface mounted (NSM) steel rebars along with fiber reinforced polymer (FRP) sheets to prevent (or diminish) the risk of progressive collapse in precast reinforced concrete (RC) beam-column joints. The study details tests involving one control specimen that is a half-scale single-story precast RC beam-column assembly having two bays. One monolithic test specimen with continuous longitudinal beam rebars was employed for comparison. The third specimen was similar to the control one, but it was retrofitted using FRP sheets combined with NSM steel rebars within the beam-column joint zone. The base of the center column was released, and a dynamic load was applied in the vertical direction on this column for simulating the column-removal scenario of progressive collapse. The proposed strengthening technique was efficient at enhancing the peak load and dissipated energy of the upgraded specimen by about 16.9 and 12.4 times, respectively, of control precast specimen. Three dimensional (3D) finite element (FE) models that consider rate-dependent material nonlinearity and bond behavior at FRP-to-concrete interface were also devised to predict the behavior of test specimens. Good agreement was obtained between the experimental and FE results with prediction errors ranging from 0% to 4%, 1% to 17%, and 3% to 10% for peak load, center column displacement at peak load, and dissipated energy at ultimate state. The validated FE models were employed for parametric studies of practical interest for investigating the impact of different strengthening parameters on the behavior of test specimen under the middle column-loss scenario.

© 2020 Elsevier Ltd. All rights reserved.

## 1. Introduction

The precast reinforced concrete (RC) building frames are in use for the past few decades. The primary reasons for their popularity in building construction are: (i) better quality control through the manufacture of structural elements in factories under controlled conditions, (ii) saving time by speeding up the construction, and (iii) saving money by reducing the material wastages and reduction in formwork cost. However, the joints in the precast construction are the weakest element, which is mainly responsible for the progressive collapse failures of these structures, such as the progressive collapse of Ronan Point building in the U.K. [1,2]. The weakness of joints in precast buildings causes a lack in continuity between structural members and hence the absence of redundancy

in the load paths. Thus, there is a need for retrofitting the beam-column connections in the existing RC buildings built using precast elements for mitigating (or minimizing) the risk of progressive collapse.

The behavior of different types of precast RC beam-column joints in buildings has been studied by many researchers [3–9]. The load–displacement response of these buildings was compared with the conventional cast-in-situ RC buildings.

The column-loss scenario is one of the common approaches adopted for checking the robustness of structures against progressive collapse. Some of the major studies in the area of progressive collapse are covered in Refs. [10–18]. Although significant research has been performed on upgrading the cast-in-situ RC beam-column connections using various methods [19–24], studies on strengthening of precast RC beam-column joints are limited [25–27].

Da Fonseca et al. [25] investigated experimentally the behavior of unstrengthened (control) as well as strengthened precast RC frames. The test assembly was a single-story and one-bay frame. The retrofitting of the beam-column connection was done through the use of near-surface mounted (NSM) carbon fiber reinforced polymer (CFRP) strips embedded in the concrete cover of the beam-column connection region. The test specimens were tested under two-point loads applied to the beam till failure. The behavior of the upgraded test specimen was found to be semi-rigid, which reduced the beam displacement substantially as compared to the control specimen.

Al-Salloum et al. [26] presented an effective technique to strengthen precast RC beam-column joints for minimizing the risk of progressive collapse in multistory buildings. Three half-scale 2D beam-column assemblies were tested. The first assembly was unstrengthened control precast specimen simulating the most common types of existing precast RC beam-column joints. The second specimen was monolithic, having continuous beam rebars. The third assembly was similar to the control one; however, it was upgraded using steel plates bolted in the joint region. It was concluded that upgrading of precast RC beam-column joints using bolted steel plates was efficient in enhancing the load resistance of the 2D assembly under column-removal scenario.

Pan et al. [27] conducted laboratory investigation on two half-scale precast RC frame sub-assemblages under a pushdown loading regime simulating column-loss scenarios in real progressive collapse conditions. One of the specimens was control (i.e., unstrengthened), whereas the second specimen was retrofitted using CFRP sheets on the side faces of the beams. Hybrid FRP anchors were used to anchor the middle portions of the CFRP sheets. The strengthening was proven to be effective up to the early catenary action (CA) stage (corresponding to the maximum pushdown displacement of 0.2$L$, where $L$ = beam span). However, when the deformation exceeded 0.2$L$, rupture of CFRP occurred gradually, and the CFRP sheets no longer contributed to the load capacity. No shearing failure was developed in the hybrid FRP anchors, which proves the efficiency of the anchorage method.

The review of available literature reveals that most of the research done on precast RC beam-column connections was in two main directions. Some researchers [28–33] developed new beam-column connections for improved seismic resistance. Other researchers [7,18,34–37] studied the progressive collapse risk of precast RC frames having either conventional or newly developed beam-column joints. However, studies on the strengthening of existing precast RC beam-column joints for improving the progressive collapse robustness of buildings are scanty [26,27]. Since precast buildings are widely used worldwide, there is an urgent need to develop methods to upgrade these buildings to increase their progressive collapse robustness. This is so crucial to avoid loss of life and property in the event of partial or total collapse. It is due

to these reasons that it is required to carry out research on the progressive collapse potential of unstrengthened as well as strengthened precast RC frames.

The focus of the present research is to study the performance of an innovative hybrid strengthening scheme composed of CFRP sheets together with NSM steel rebars to upgrade precast RC beam-column joints for mitigating (or minimizing) the progressive collapse risk in multistory buildings. The novelty of this research is originated from the fact that this strengthening technique has not been used before in upgrading of precast RC beam-column joints for reducing the risk of progressive collapse due to column-loss events. Three specimens of 2D beam-column assemblages were tested for simulating the progressive collapse due to the loss of a column. Two test specimens were precast, whereas the third specimen was monolithic, having continuous longitudinal rebars in beams. One of the precast specimens was control, and the other one was strengthened using the hybrid scheme. In addition to the tests, 3D finite element (FE) models that take into account the rate-dependent material nonlinearity and contact behavior at FRP-to-concrete interface were devised using LS-DYNA package [38] for predicting the behavior of test specimens under column-loss scenario. The validated FE models were employed for parametric studies of practical interest for investigating the impact of different strengthening parameters on the behavior of test specimen under the middle column-missing scenario.

## 2. Experimental program

### 2.1. Test matrix

Three test specimens of beam-column assemblages (single story with two bays) were tested for the loss of the middle column. The test specimens – with regard to reinforcement detailing and geometric dimensions – were selected to be half scale of a two-bay prototype perimeter frame, which was taken as a portion from an existing precast RC building in Saudi Arabia. One of the specimens was precast control (PC-C), which was detailed to simulate the prevalent precast construction practices in Saudi Arabia. The second specimen (MC-SMF) had the same dimensions, but it was built with monolithic beam-column connection having continuous beam rebars. The remaining test specimen (PC-S) was the strengthened precast assembly. Strengthening of the beam-column joints was done using a combination of CFRP sheets and NSM steel rebars.

### 2.2. Details of test specimens

Figs. 1–3 show the dimensions and detailing of reinforcement in the tested specimens, which were the same for the two precast specimens PC-C and PC-S. The beams and columns had the same section dimensions (350 × 350 mm). The column height, measured to the soffit of the beam, was 1050 mm. The test specimens were resting on steel stubs supported on steel I-sections attached to the strong lab floor (see Figs. 4 and 5). The beams were reinforced with 4 φ16 mm rebars in tension as well as compression. The shear reinforcement was in the form of two-legged shear stirrups of φ8 mm rebars provided at a center-to-center spacing of 100 mm. The RC columns were reinforced with 8 φ16 mm longitudinal rebars, with φ8 mm ties provided at a center-to-center spacing of 100 mm (Fig. 1). The complete details of casting and fabrication of precast connection can be seen in Refs. [26,39]. The longitudinal beam rebars were continuous in the connection region of monolithic specimen MC-SMF (see Fig. 2), whereas other details were the same as specimen PC-C.
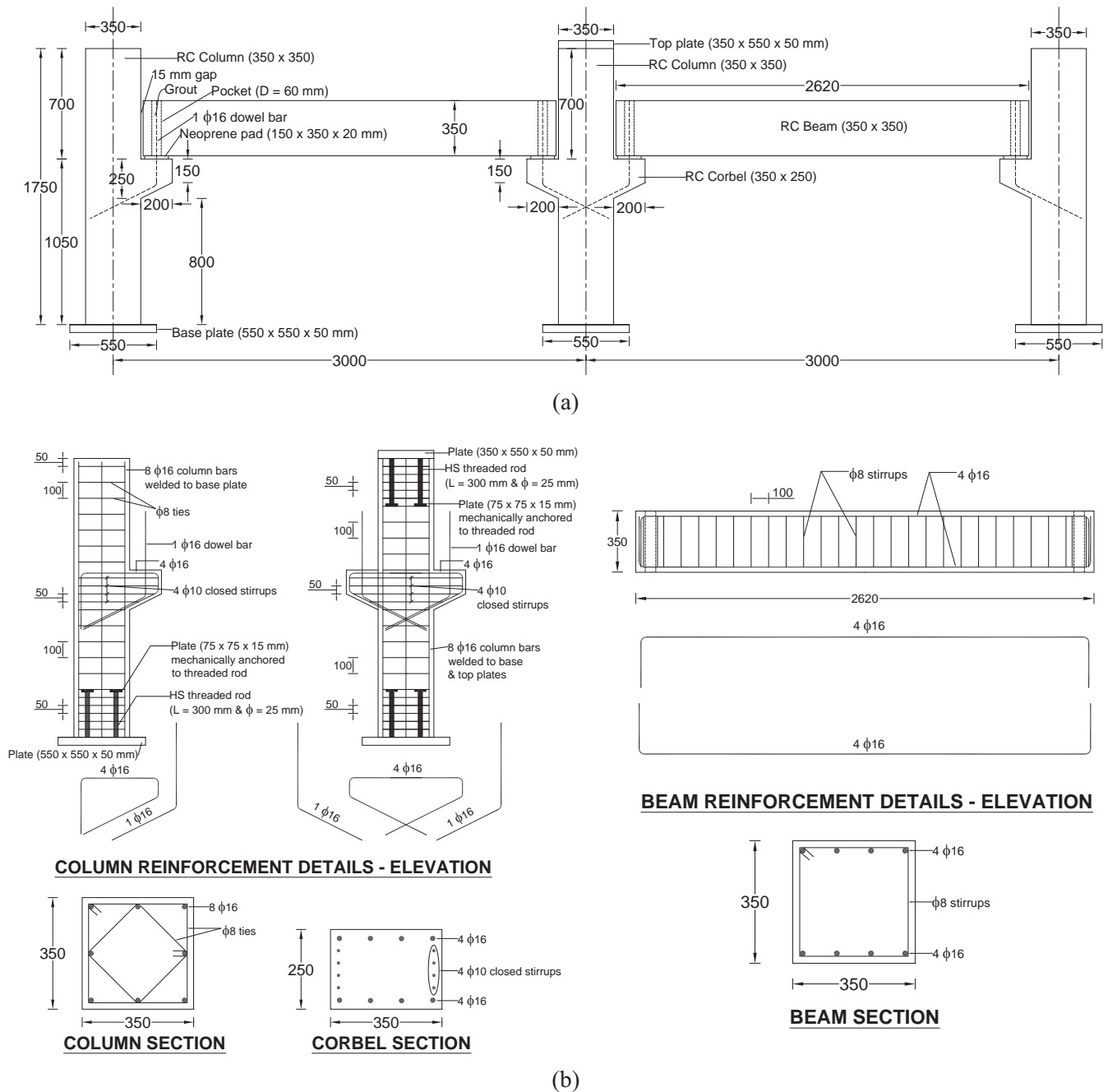
**Fig. 1.** Details of precast specimen PC-C (Note: All dimensions are in mm): (a) Test specimen; (b) Reinforcement details.

Details of the strengthening scheme for specimen PC-S are shown in Fig. 3. Specimen PC-S had 4 φ12 mm NSM steel rebars placed in grooves that were filled with epoxy adhesive mortar. There were four grooves on each side of the connection zone. Two grooves were located at 40 mm from the top and bottom of the beam, and the middle two grooves had a clear spacing of 50 mm, as seen in Fig. 3. These grooves had dimensions of 30 × 25 mm along the connection region in the lateral concrete cover. The NSM rebars were covered with two layers of externally bonded CFRP composites (one horizontal and one vertical) on each side of the connection region. The approach adopted to come up with this innovative design of using NSM steel rebars in combination with externally bonded CFRP sheets can be explained as follows.

Once a column is abruptly removed in an extreme case, such as the blast load, the load carried by such a column should be redistributed to the neighboring columns via the beam-column connection. The vertical dynamic load will then be transferred to the beam through the direct shear at the column face. Since the CFRP sheets cannot be relied upon for resisting the direct shear transmitted at the beam-column interface, NSM steel rebars were used for this purpose. The horizontal CFRP sheets combined with NSM steel rebars were designed to have a beam section with flexural capacity approximately the same as that of the beam section of monolithic specimen MC-SMF. Ignoring concrete contribution to shear strength, the vertical CFRP reinforcement was designed to give shear strength of beam at the connection region that exceeds the flexural capacity of the upgraded section. Owing to the
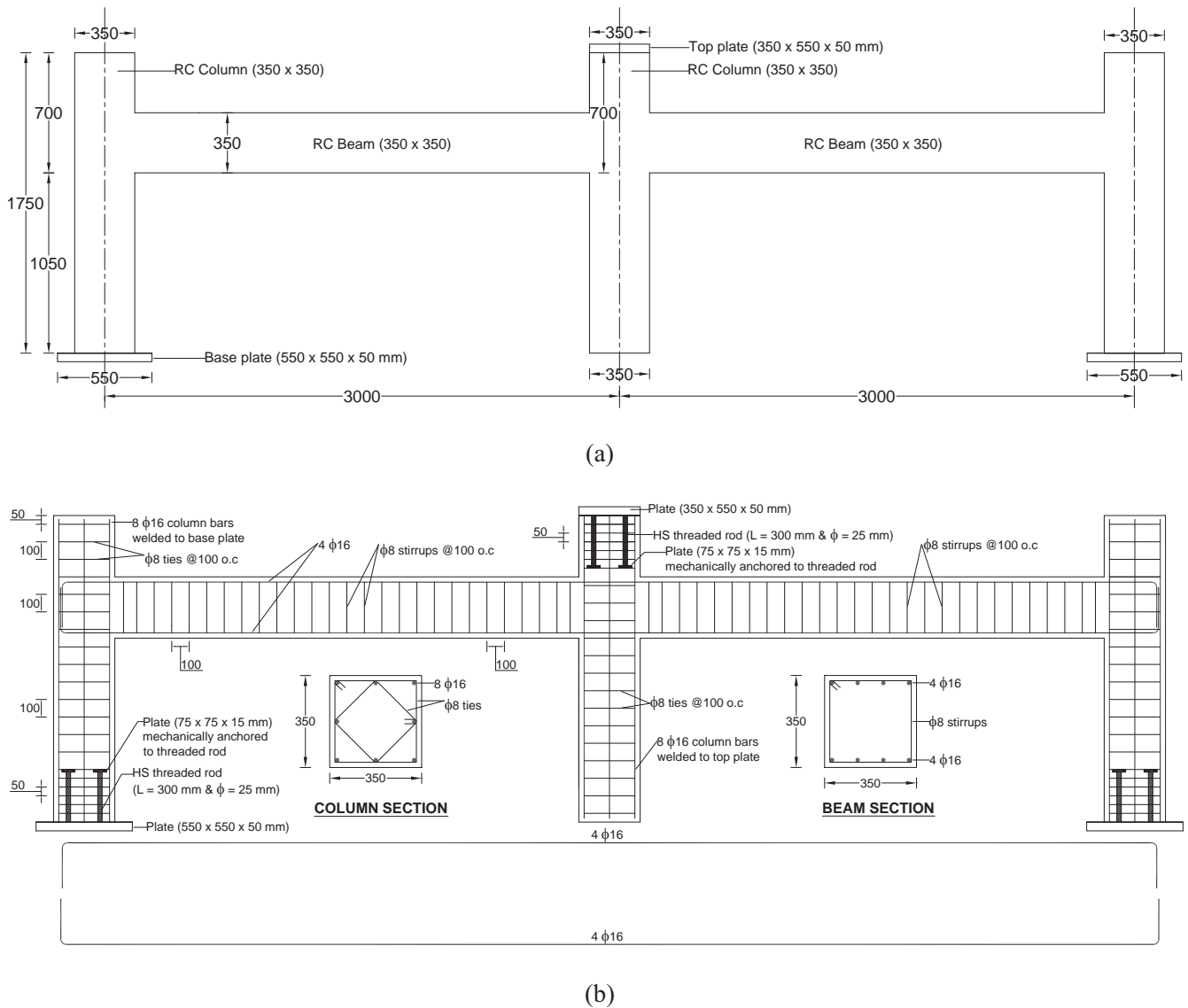
(a)



(b)

**Fig. 2.** Details of monolithic specimen MC-SMF (Note: All dimensions are in mm): (a) Test specimen; (b) Reinforcement details.

presence of corbels at beam ends, the vertical CFRP reinforcement was only provided at the sides of the beam until it became in the form of U-shape beyond the corbel face (see Fig. 3). In order to comply with the requirements of the ACI 318–19 code [40] for special moment resisting frames, the plastic hinge regions were covered by extending the strengthening layers over a distance equal to twice the beam depth beyond the column face. This also satisfied the tension development length of the NSM rebars.

The assembly of the precast RC specimen PC-S was performed as it is done in the construction field [26,39]. After the assembly, the surfaces of the beam-column regions were roughened using sandblasting to have a sound bond between CFRP sheets and concrete substrate. Three beam-column connections were strengthened using NSM steel rebars placed in grooves that were cut along each side of the connection region in the lateral concrete cover. A special concrete saw was used to cut the grooves on the lateral surfaces of the beams and columns. The grooves were cleaned by removing dust with the help of compressed air and cleaned subsequently using acetone. Fig. 4(a) shows grooves for the three connections. The steel rebars were then introduced in the grooves, which were filled with epoxy mortar, as seen in

Fig. 4(b). After curing of the mortar within the grooves, CFRP sheets were bonded to the concrete surface with two-part epoxy. The steps involved for the strengthening of the test specimen PC-S are shown in Fig. 4.

*2.3. Material properties*

The properties of different materials employed in the preparation of test specimens are listed in Table 1. The average concrete strength obtained by testing standard cylinders (150 × 300 mm), according to ASTM C39 [41], on the day of testing the specimens was 37.3 MPa. The locally available material, Sika Grout 214, was used for grouting. The compressive strength of the grout was found by testing 50-mm cubes according to the test standard in Ref. [42]. The steel rebars of all diameters were tested in tension following the test standard in Ref. [43], and the mechanical properties obtained through these tests are listed in Table 1. CFRP sheets employed in this research were unidirectional. Tensile tests, according to the relevant test standard [44], were performed on test coupons of the CFRP sheet. Table 1 provides properties of the CFRP composite system. The structural two-part epoxy mortar
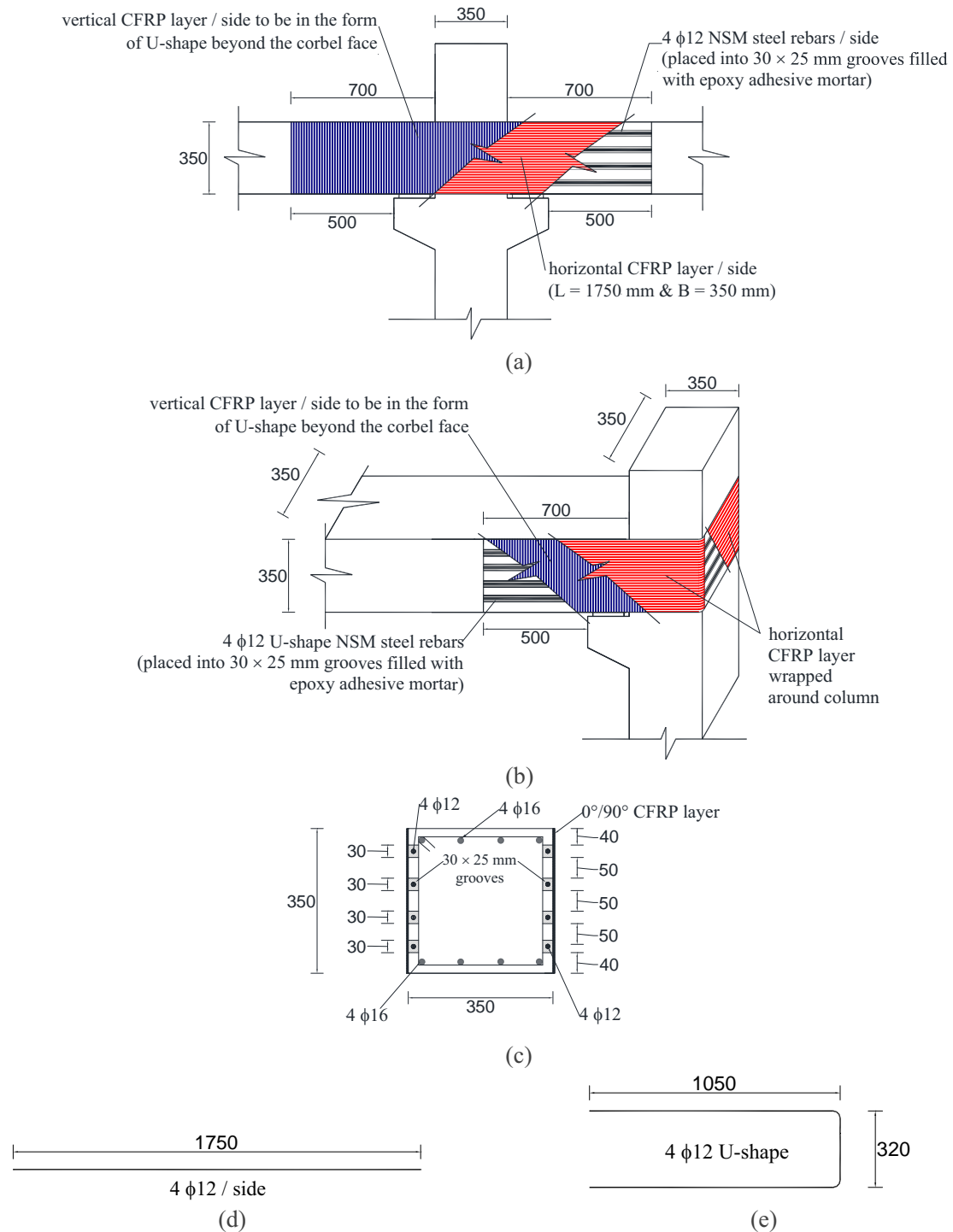
**Fig. 3.** Details of strengthened specimen PC-S (Note: All dimensions are in mm): (a) Middle joint; (b) Outer right joint; (c) Cross section of strengthened beam; (d) NSM rebars for middle joint; (e) NSM rebars for outer right joint – plan view.

(Sika 31) was used for filling the grooves of NSM rebars. Table 1 lists the compressive strength of the epoxy adhesive mortar as given by the manufacturer.

*2.4. Test protocol*

Fig. 5 shows the test setup used for testing the specimens. The progressive collapse of building frames was simulated by taking out the support of the middle column and applying a dynamic downward load on such a column using a high-speed servo-control MTS actuator. The actuator was utilized to apply the load on the middle column in cycles of incremental vertical displacement, as seen in Fig. 6. Unloading of test specimens was conducted by taking the middle column from its displaced position to its initial position prior to the onset of the test. The rest period was used for marking the cracks and recording observations. It is worth mentioning that the actuator load was applied at a rate of 100 mm/s, while the unloading was conducted at a much slower
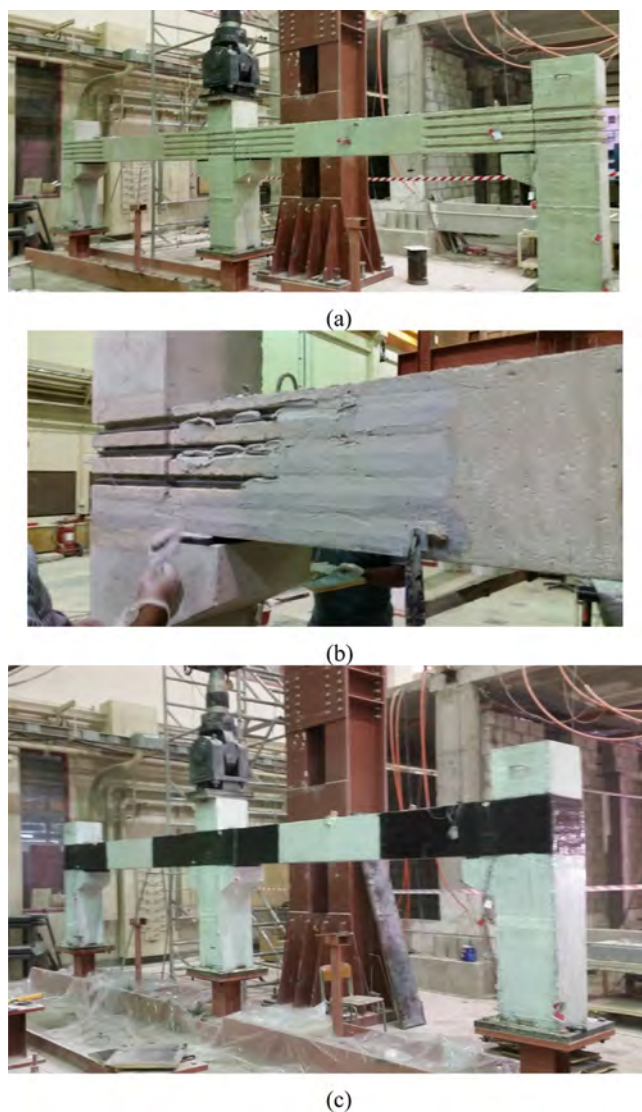
Fig. 4. Steps involved in strengthening of specimen PC-S: (a) Grooves along connection region; (b) Affixing NSM steel rebars and filling up grooves with epoxy adhesive mortar; (c) Installation of CFRP sheets.

rate of 5 mm/s. The test data were collected at a frequency of 1 k/s. The instrumentation of test specimen includes: (i) strain gages to measure strains in steel rebars and CFRP sheets at critical locations, (ii) laser transducers to measure beam displacements, (iii) inclinometers to measure joint rotations, and (iv) load cell to measure actuator load. The details of the instrumentation of the precast specimen PC-C are shown in Fig. 5.

## 3. Discussion of experimental results

Table 2 provides a summary of the key parameters of the experimental results of the tested specimens. It is important to note that the ultimate limit state is taken as the post-peak state when the drop in load reaches 20% of the peak load [45].

### 3.1. Modes of failure

Fig. 7(a) to (c) show the final failure modes of the test specimens PC-C, MC-SMF, and PC-S, respectively. The failure of the control test specimen PC-C was through concrete crushing at beam ends, which was caused by the rotation of beam ends, as shown

in Fig. 7(a). However, the failure of test specimen MC-SMF was through the development of plastic hinges (denoted by wide flexural cracks in the tension zone and concrete crushing in the compression zone) at beam ends, as seen in Fig. 7(b). The flexural cracks were also observed in the end columns, which was due to the rotation of end columns. The catenary action could not be developed due to: (i) insufficient restraint provided by the end columns, (ii) discontinuity of beams at the ends, (iii) discontinuity of columns due to the consideration of a single story, and (iv) absence of column axial load. These limitations helped in representing the worst-case scenario of progressive collapse in existing multistory buildings.

Fig. 7(c) shows the final deformed state and mode of failure for specimen PC-S. The failure started in the beam around the inner beam-column connection due to the rupture of horizontal CFRP sheets at the bottom edge together with fracture of extreme bottom NSM rebars near the column face, as shown in Fig. 7(c). It should be noted that due to the propagation of flexural cracks in the maximum-moment zone at column face, the rupture of horizontal CFRP sheets was initiated at the extreme bottom edge then extended upward to the extreme top edge, as seen in Fig. 7 (c). In addition, the crushing of concrete was noticed at the top beam side near the middle connection zone, as depicted in Fig. 7(c). It should be noted that the single layer of transverse CFRP U-wrap was about 32% of that required by Eq. (14.1.2) of the ACI guidelines [46], and it proved to be efficient in inhibiting the unwanted failure modes in the CFRP sheets around the middle connection zone such as the delamination of concrete cover and FRP interfacial end debonding. This was also supported in an earlier study by Almusallam et al. [47]. Failure of exterior beam-column connection occurred at a later stage towards the end of the test due to CFRP end interfacial debonding (see Fig. 7(c)). This failure took place in the concrete layer close to the concrete/adhesive interface, and it was thought to be owing to high normal and interfacial shear stresses close to the CFRP ends that exceed the concrete strength [48]. Debonding commenced at the end of the CFRP sheet and propagated along the interface of concrete and CFRP towards the beam-column joint zone without reaching the level of NSM steel reinforcement, as shown in Fig. 7(c). This debonding failure is less common than the well-known concrete cover delamination failure, and its mechanism is complicated [49]. CFRP debonding failure mode was noticed at exterior joints due to the insufficient anchorage provided at the ends of CFRP sheets. The provided U-wrapped CFRP layer could not provide adequate anchorage for the horizontal CFRP layer in the negative-moment region, as the flexural cracks are initiated at the top edge of the beam at which the vertical CFRP layer is discontinuous. Proper anchorage could have been achieved by the provision of full wrapping (if possible), mechanical fasteners, fiber anchors, or bolted steel plates at CFRP ends, which have been proven in the literature to be successful at delaying, and sometimes preventing, debonding failure of the longitudinal FRP layers [50–52]. For example, Bengar and Shahmansouri [52] have recently proposed a new anchorage system for CFRP strips in externally strengthened RC continuous beams. The proposed anchorage system consisted of steel plates and bolts and has led to a considerable increase in the loading capacity, moment redistribution ratio, and ductility in comparison with the CFRP-strengthened beams without the anchorage.

For strengthened specimen PC-S, it was noted from the visual inspection of both interior and exterior joints at failure that debonding was not noticed at epoxy mortar/concrete and NSM rebars/epoxy mortar interfaces (see Fig. 7(c)). As seen from Table 1, the epoxy adhesive mortar has high bond strength with steel rebars (=12 MPa), which justifies the perfect bond noticed during the experiment.
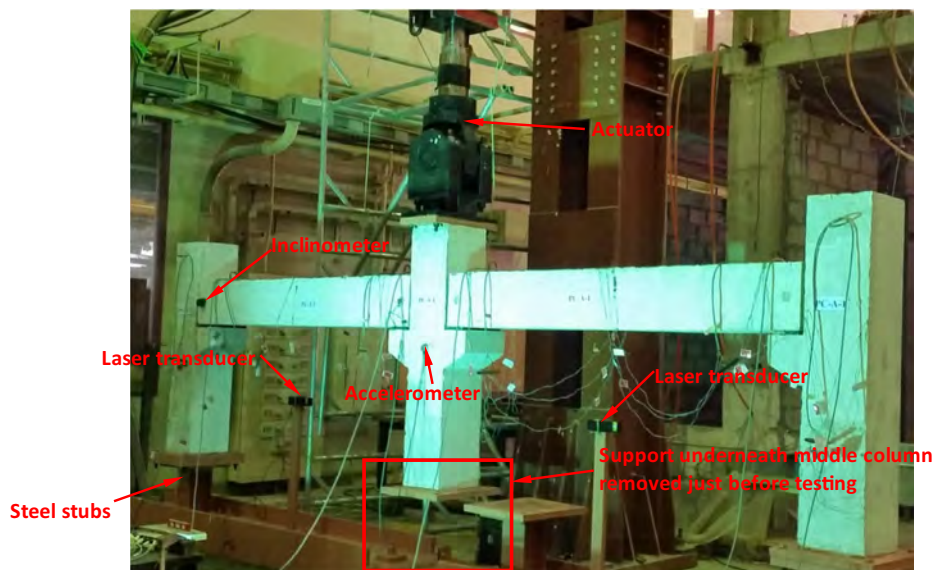
**Fig. 5.** Test setup and instrumentation layout for specimen PC-C.

**Table 1**
Material properties used in the FE modelling.

| | φ8 | φ10 | φ12 | φ16 | Threaded rods | Plates |
|---|---|---|---|---|---|---|
| *Concrete & cementitious grout* | | | | | | |
| Material model | Type 159 (MAT_CSCM_CONCRETE) | | | | | |
| Density (kg/m³) | 2320 | | | | | |
| Uni-axial compressive strength (MPa) | 37.3 for concrete & 60 for cementitious grout | | | | | |
| *Epoxy mortar* | | | | | | |
| Material model | Type 159 (MAT_CSCM_CONCRETE) | | | | | |
| Density (kg/m³) | 2320 | | | | | |
| Uni-axial compressive strength (MPa) | 65 | | | | | |
| Tensile strength (MPa)* | 21 | | | | | |
| Bond strength with steel (MPa)* | 12 | | | | | |
| *Steel rebars, threaded rods & plates* | φ8 | φ10 | φ12 | φ16 | Threaded rods | Plates |
| Material model | Type 24 (MAT_PIECEWISE_LINEAR_PLASTICITY) | | | | | |
| Density (kg/m³) | 7850 | | | | | |
| Young's modulus (GPa) | 200 | | | | | |
| Poisson's ratio | 0.3 | | | | | |
| Strain rate parameter, C | 250 | | | | | |
| Strain rate parameter, $p$ | 1.6 | | | | | |
| Yield stress (MPa) | 525 | 489 | 569 | 526 | 350 | 250 |
| Tangent modulus (MPa) | 127 | 2127 | 862 | 1065 | 0 | 0 |
| Plastic strain to failure (%) | 19.7 | 11.6 | 11.7 | 11.7 | 19.8 | 19.9 |
| *Neoprene pads* | | | | | | |
| Material model | Type 77 (MAT_HYPERELASTIC_RUBBER) | | | | | |
| Density (kg/m³) | 1100 | | | | | |
| Poisson's ratio | 0.499 | | | | | |
| Shear modulus (MPa) | 1.38 | | | | | |
| Limit stress (MPa) | $5.52 \times 10^{-3}$ | | | | | |
| Constant $C_{10}$ | 0.55 | | | | | |
| Constant $C_{01}$ | 0 | | | | | |
| Constant $C_{11}$ | 0 | | | | | |
| Constant $C_{20}$ | −0.05 | | | | | |
| Constant $C_{02}$ | 0 | | | | | |
| Constant $C_{30}$ | 0.95 | | | | | |
| *CFRP material* | | | | | | |
| Material model | Type 54–55 (MAT_ENHANCED_COMPOSITE_DAMAGE) | | | | | |
| Density (kg/m³) | 1740 | | | | | |
| Thickness per layer (mm) | 1.0 | | | | | |
| Young's modulus in long. dir. (GPa) | 95.8 | | | | | |
| Young's modulus in transverse dir. (GPa) | 4.2 | | | | | |
| Longitudinal tensile strength (MPa) | 958 | | | | | |
| Transverse tensile strength (MPa) | 95.8 | | | | | |
| *Steel stubs at base of columns* | | | | | | |
| Material model | Type 1 (MAT_ELASTIC) | | | | | |
| Density (kg/m³) | 7850 | | | | | |
| Young's modulus (GPa) | 200 | | | | | |
| Poisson's ratio | 0.3 | | | | | |

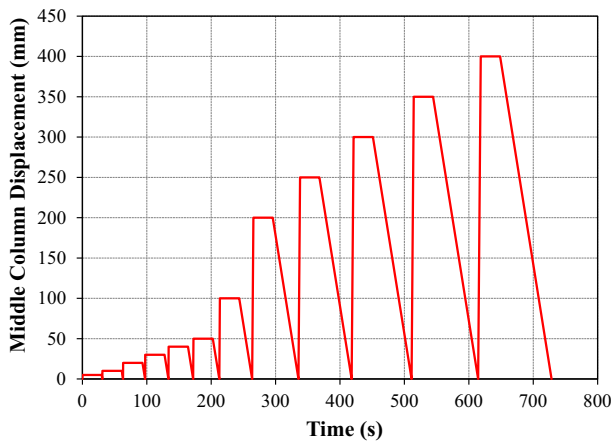*This property was not input in the FE modeling; however, it was listed for reference.

**Fig. 6.** Target middle column displacement vs. time history for testing of specimens.

### 3.2. Load-displacement response

Fig. 8(a) to (c) show the load–displacement hysteresis for the test specimens PC-C, MC-SMF, and PC-S, respectively. The envelopes of the load–displacement hysteresis are also plotted in these figures. These envelopes are plotted together in Fig. 8(d) for comparison. As expected, the vulnerability of the control test specimen PC-C is evident from Fig. 8(a), as the peak load is very low (12.8 kN). The load–displacement behavior of test specimen MC-SMF (Fig. 8(b)) can be divided into four different stages, namely, (i) elastic stage (segment AB), (ii) inelastic stage (segment BC), representing a reduction of secant stiffness, (iii) plastic hinge rotation stage (segment CD), representing the formation of plastic hinges at ends of beams until the onset of the drop in progressive collapse resistance, which started to occur after a middle column displacement of 250 mm (approx.), and (iv) onset of catenary action stage (portion DE) representing the initiation of catenary action through the development of tensile stresses in the top rebars of beams at middle column; nevertheless, due to the limitation outlined above, catenary action was not fully developed. The same results were confirmed in a previous experimental and FE study conducted by the authors [53] on progressive collapse risk of RC special moment resisting frame (SMRF) assemblies. In the previous study, the catenary action phase was not developed in assemblies without column continuity (single-story specimens). However, the provision of continuity in beams and columns favored the full development of the catenary action phase. As compared to the control precast specimen, the monolithic test specimen MC-SMF resisted a much

higher load (17.8 times the control specimen PC-C, as seen in Table 2), and the energy dissipated up to the ultimate state was also very high.

The load–displacement envelope of the strengthened specimen PC-S (Fig. 8(c)) also shows four different stages of behavior. The first stage is the elastic stage represented by segment AB (Fig. 8 (c)). The second stage is the inelastic stage represented by segment BC. It is observed from the recorded rebar strains at the inner column face that all NSM steel rebars in the tension side of the beam had already yielded at point C; however, tension NSM rebars at the faces of outer columns showed no yielding. The third stage is the flexural action zone (segment CD), during which crushing of concrete occurred in the compression zone of beams near the middle joint, and it was associated with fracture of bottom NSM rebars as well as rupture of CFRP sheets near the inner connection. Due to the fracture of bottom NSM rebars and the rupture of the horizontal CFRP layer near the middle joint, there is no catenary behavior in the DE segment (fourth stage). Retrofitting of precast beam-column connections using the innovative CFRP/NSM hybrid technique was found to significantly enhance the load–displacement characteristics under the column-removal scenario. The ultimate load of upgraded specimen PC-S was about 16.9 times of the control specimen PC-C. Displacement ductility and energy dissipated were also remarkably increased due to strengthening.

It should be noted that the displacement ductility listed in Table 2 is defined as the ratio of middle column displacement at the ultimate state to the middle column displacement at first yielding of bottom beam rebars at the inner joint. Due to the discontinuity of beam rebars at joint regions for control specimen PC-C, the recorded strain at peak load for beam bottom rebars at the inner column face was 74 $\mu\varepsilon$ (see Table 2), which is significantly less than the yield strain (=2630 $\mu\varepsilon$). Consequently, there is no yield displacement and hence no displacement ductility for specimen PC-C. A displacement ductility of 5.4 was calculated for specimen PC-S compared with no ductility at all for control test specimen PC-C. The energy absorbed at the ultimate state of specimen PC-S was about 12.4 times the control test specimen PC-C. As compared with monolithic specimen MC-SMF, strengthened specimen PC-S had a peak load of about 95% of that of specimen MC-SMF. Yet, displacement ductility and energy dissipated at the ultimate state of test specimen PC-S were 51% and 53%, respectively, of those for monolithic specimen MC-SMF.

## 4. Numerical FE modeling

LS-DYNA software [38] was employed for the numerical modeling of RC test specimens. Only one-half of the specimen was modeled due to its symmetry.

**Table 2**
Comparison of experimental and FE results for test specimens*

| Specimen ID | Results | $P_u$ (kN) | $\Delta_{u,c}$(mm) | $P_y$ (kN) | $\Delta_y$(mm) | $\Delta_u$(mm) | $\mu_\Delta$ | $E_u$ (kN.m) | $\varepsilon_{sb,bot}$ ($\mu\varepsilon$) | $\varepsilon_{NSM,bot}$ ($\mu\varepsilon$) | $\varepsilon_{FRP,bot}$ ($\mu\varepsilon$) |
|---|---|---|---|---|---|---|---|---|---|---|---|
| PC-C | EXP | 12.8 | 145 | NY | NY | 265 | – | 2.5 | 74 | – | – |
|  | FE | 12.8 | 160 | NY | NY | 243 | – | 2.6 | 58 | – | – |
|  | EXP/FE | 1.00 | 0.91 | – | – | 1.09 | – | 0.97 | 1.28 | – | – |
| MC-SMF | EXP | 228 | 144 | 145 | 26 | 269 | 10.5 | 59 | 94,921 | – | – |
|  | FE | 218 | 145 | 153 | 21 | 335 | 16.3 | 65 | 81,911 | – | – |
|  | EXP/FE | 1.04 | 0.99 | 0.95 | 1.25 | 0.80 | 0.64 | 0.90 | 1.16 | – | – |
| PC-S | EXP | 216 | 94 | 151 | 27 | 145 | 5.4 | 31 | NA | 12,625 | 11,133 |
|  | FE | 217 | 80 | 146 | 32 | 154 | 4.9 | 29 | 1393 | 13,184 | 10,785 |
|  | EXP/FE | 0.99 | 1.17 | 1.04 | 0.85 | 0.94 | 1.11 | 1.06 | – | 0.96 | 1.03 |

*$P_u$ = peak load; $\Delta_{u,c}$ = middle column displacement at peak load; $P_y$ & $\Delta_y$ = load and middle column displacement at first yielding of main beam steel at inner column face (bottom rebars for specimen MC-SMF & bottom NSM rebars for specimen PC-S); $\Delta_u$ = middle column displacement at ultimate state; $\mu_\Delta$= displacement ductility = $\Delta_u/\Delta_y$; $E_u$ = energy dissipated at ultimate state, $\varepsilon_{sb,bot}$ = strain at peak load for beam bottom rebars at inner column face; $\varepsilon_{NSM,bot}$ = strain at peak load for bottom NSM steel rebars at inner column face; $\varepsilon_{FRP,bot}$ = strain at peak load for bottom edge of horizontal CFRP sheets at inner column face; EXP = experimental; FE = finite element; NY = No steel yielding; NA = not available data.
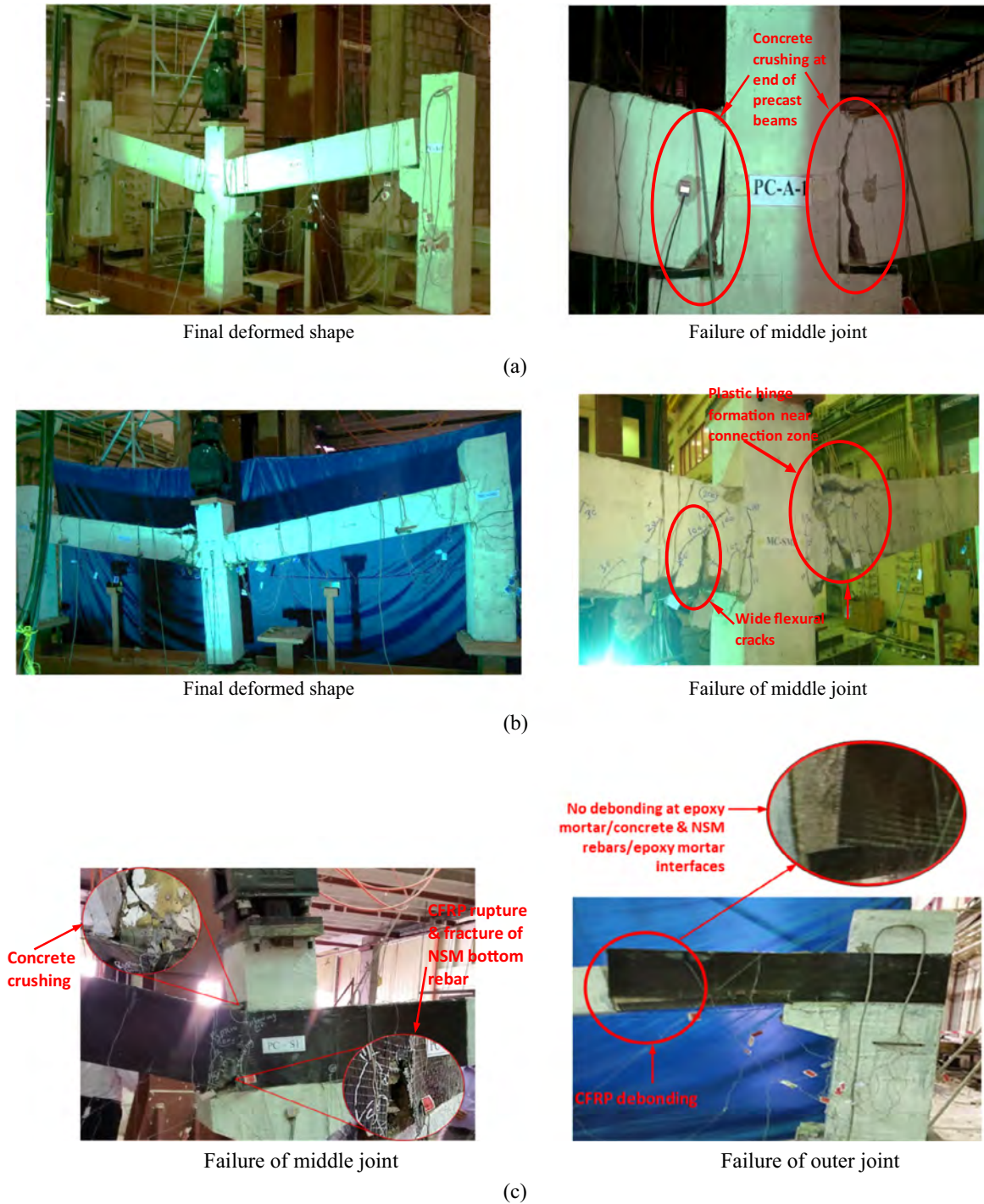
Final deformed shape

Failure of middle joint

(a)

Final deformed shape

Failure of middle joint

(b)

Failure of middle joint

Failure of outer joint

(c)

**Fig. 7.** Mode of failure for: (a) Precast specimen PC-C; (b) Monolithic specimen MC-SMF; (c) Strengthened specimen PC-S.

### 4.1. FE mesh

Fig. 9(a), 9(b), and 10 show FE mesh discretization of the three test specimens, namely, PC-C, MC-SMF, and PC-S, respectively. The concrete in all test specimens, neoprene pads in specimens PC-C and PC-S, and epoxy adhesive mortar in specimen PC-S were modeled using eight-node solid elements. The steel rebars used in different structural elements were modeled using two-node beam elements. The CFRP sheets of specimen PC-S were modeled using four-node shell elements [54]. The size of the beam, solid and shell elements varied from 2.5 to 50 mm. The mesh size was decided

based on the mesh sensitivity study. It was found that any further refinement was not practically useful, as it may increase the solution time significantly. Some highlights on size calibration for steel elements are given in the following subsection.

### 4.2. Material models

The strain-rate effect arising due to the application of dynamic load was incorporated in the material models. Concrete, cementitious grout, and epoxy mortar were modeled using model type 159 [55]. For model type 159, the viscoplastic rate effects were
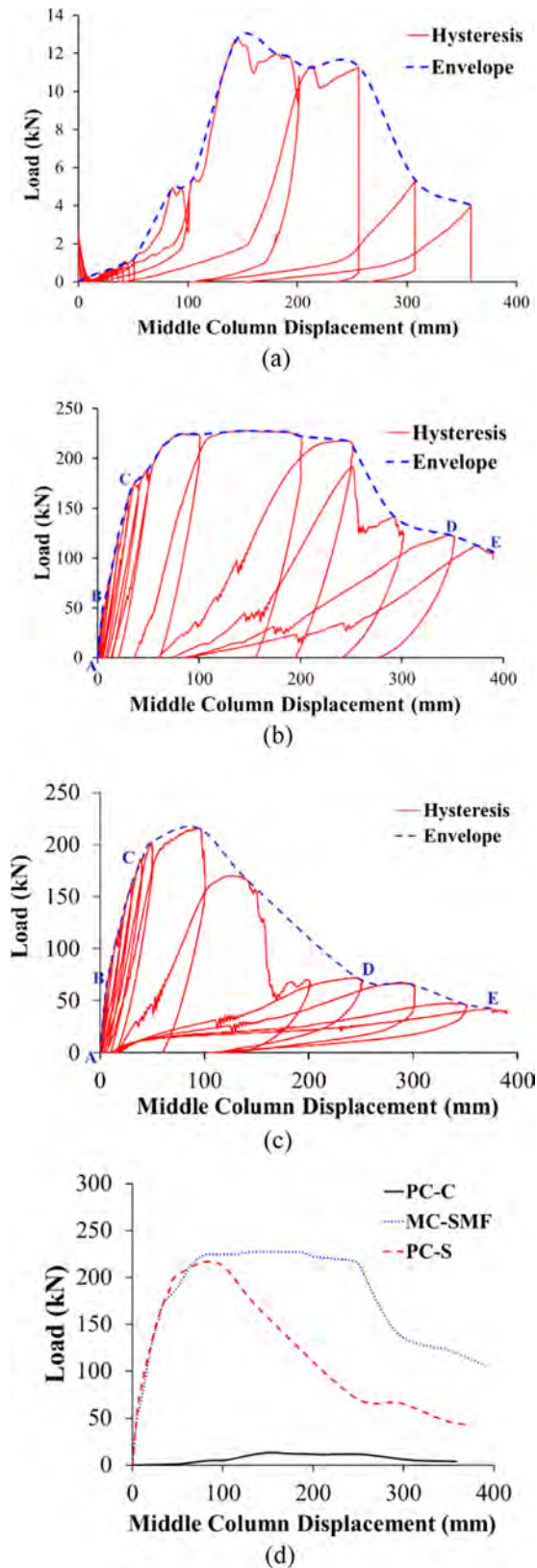
**Fig. 8.** Load-displacement curves for tested specimens: (a) Hysteresis loops for specimen PC-C; (b) Hysteresis loops for specimen MC-SMF; (c) Hysteresis loops for specimen PC-S; (d) Load-displacement envelope comparison.

included in the FE analysis. The stress at each time step $\Delta t$ is updated from the strain-rate increments using an incremental

form of Hooke's Law. This updated stress is termed as the trial elastic stress $\sigma_{ij}^T$, and if it lies on or inside the yield surface, the performance is considered elastic, and the plasticity algorithm is evaded. Nevertheless, if the trial elastic stress state lies outside the yield surface, the performance is considered elastic–plastic (with possible hardening, damage, and rate effects), and the stress state goes back to the yield surface via the plasticity algorithm. This elastic–plastic stress is termed as inviscid stress $\sigma_{ij}^p$. The viscoplastic stress (including rate effects) at each time step, $\sigma_{ij}^{vp}$, is calculated from

$$\sigma_{ij}^{vp} = (1 - \gamma)\sigma_{ij}^T + \gamma\sigma_{ij}^p \tag{1}$$

with

$$\gamma = \frac{\Delta t/\eta}{1 + \Delta t/\eta} \tag{2}$$

where $\eta$ is the effective fluidity factor, which is internally computed in LS-DYNA using the strain rate $\dot{\varepsilon}$.

The steel rebars of different members as well as the NSM rebars of specimen PC-S were simulated with the help of material model type 24. The following Cowper-Symonds formulation was employed for modeling strain-rate effect in the yield stress of steel rebars:

$$y = 1 + \left(\frac{\dot{\varepsilon}}{C}\right)^{1/p} \tag{3}$$

where $y$ is the magnification factor for the yield stress, and $C$ (=250 taken in the study), and $p$ (=1.6 taken in the study) are the model parameters. For modeling of CFRP sheets of strengthened specimen PC-S, the enhanced composite damage model type 54–55 was employed along with Chang and Chang failure criteria [56]. The neoprene pads of precast specimens PC-C and PC-S were modeled using the hyperelastic rubber material model type 77 (described by Christensen [57]). Table 1 lists the properties of different materials employed in the numerical analysis.

The material failure of concrete, cementitious grout, and epoxy mortar was simulated with the help of erosion, which was based on the strain-dependent criteria. The threshold maximum principal tensile strain for the erosion of elements was adopted as 5% [55,58]. This helped in avoiding severe element distortions and deformations. The failure of steel rebars was represented by failure plastic strain. For the assessment of the input parameters for material model type 24 (presented in Table 1), standard tests were carried out on tensile coupons of steel rebars of different diameters as per Ref. [43]. The results of each test are engineering stress versus strain relationships. LS-DYNA [38] was utilized to develop FE models for the standard tests of tensile steel coupons using two-node beam elements. For such elements, the engineering stress versus strain curve in the models cannot be directly transformed to the true stress versus effective plastic strain relationship as the cross-sectional area of the beam element remains unchanged (true stress is the same as engineering stress in this case). The size of the beam elements was calibrated by the iterative analysis, and it was adjusted until a quantitative match of the experimental and numerical engineering stress–strain relationship was obtained. The observed steel fracture in the coupons was modeled by element erosion via the plastic strain to failure. The calibrated element size was then utilized in the 3D FE modeling of the test specimens, especially at critical locations of plastic hinges.

### 4.3. Contact modeling

For all test specimens, the bond between steel rebars and surrounding concrete was assumed as perfect. In testing of specimen PC-S, debonding was neither noticed between epoxy mortar and
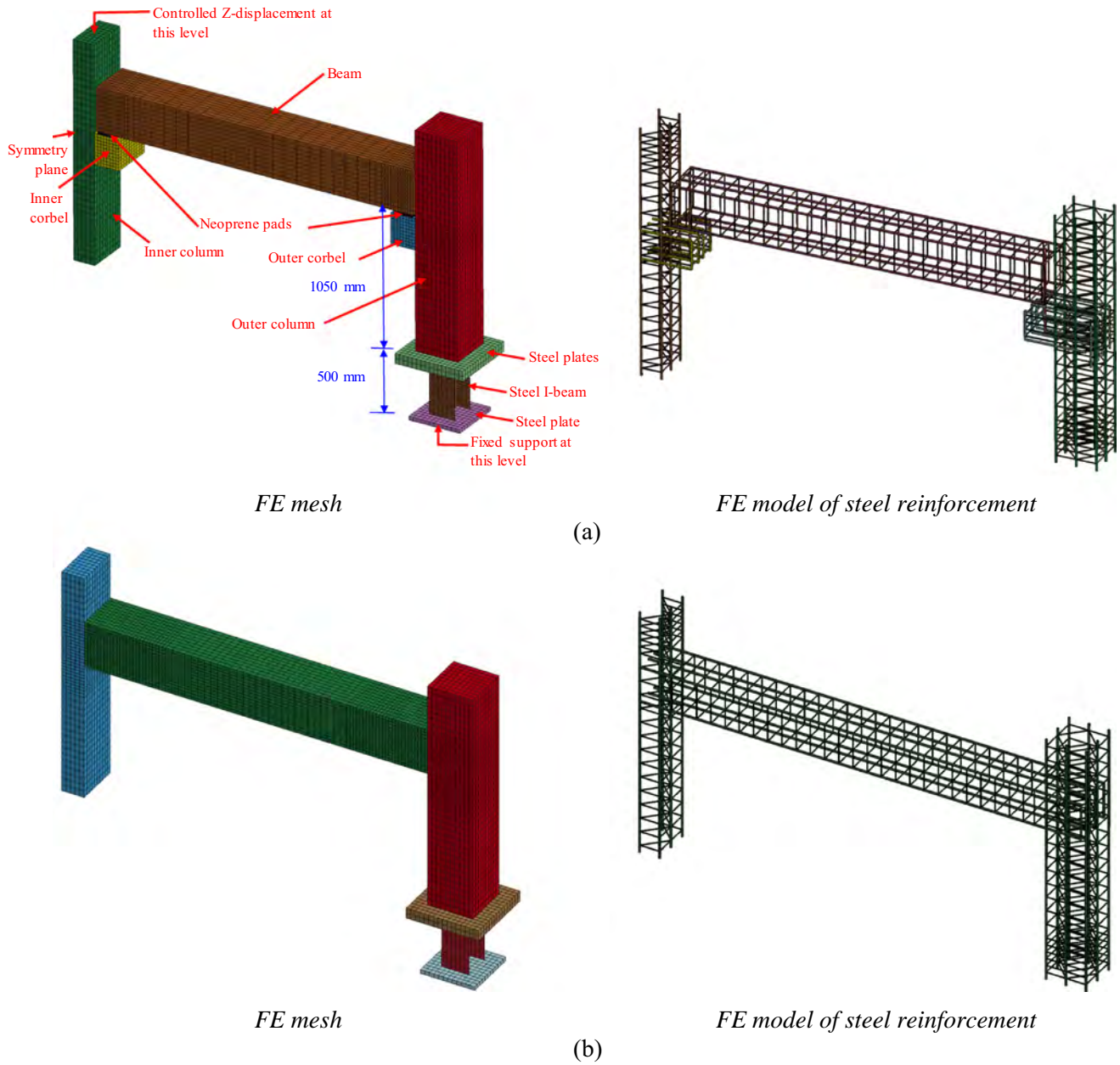
*FE mesh* — *FE model of steel reinforcement*

(a)



*FE mesh* — *FE model of steel reinforcement*

(b)

**Fig. 9.** FE model for one-half of: (a) Specimen PC-C; (b) Specimen MC-SMF.

NSM rebars nor between epoxy mortar and surrounding concrete. Thus, the bond between NSM rebars and epoxy mortar as well as between epoxy mortar and concrete was also assumed as perfect. For precast specimens, PC-C and PC-S, the interaction at contact surfaces between beam and columns, and neoprene pad and beams/corbels were modeled using general automatic surface-to-surface contact definition of LS-DYNA. The friction coefficient between concrete surfaces was taken as 0.6 [40], whereas the friction coefficient between neoprene pads and concrete surfaces was taken as 0.4 [59]. For specimen PC-S, bond at FRP-to-concrete interface was modeled using the tiebreak surface-to-surface contact of LS-DYNA, as per the following bond strength failure criterion:

$$\left(\frac{|\sigma_s|}{\sigma_{s,F}}\right)^2 + \left(\frac{|\sigma_n|}{\sigma_{n,F}}\right)^2 \geqslant 1 \tag{4}$$

where $\sigma_s$ and $\sigma_n$ are, in turn, the shear and normal stresses. Yet, $\sigma_{s,F}$ and $\sigma_{n,F}$ are the shear and normal stresses at failure, respectively, calculated from [60,61]:

$$\sigma_{s,F} = 1.5\beta_w\sigma_{n,F} \tag{5}$$

$$\sigma_{n,F} = 0.62\sqrt{f'_c} \text{ (Units : MPa)} \tag{6}$$

where $f'_c$ is the specified concrete strength and $\beta_w$ is a width correction factor estimated from

$$\beta_w = \sqrt{\frac{2.25 - b_f/b_c}{1.25 + b_f/b_c}} \tag{7}$$

where $b_c$ is the beam width, and $b_f$ is the width of CFRP sheet. It should be noted here that the contact model utilized in this research has been calibrated in previous work [47,58,62].

### 4.4. Loading strategy and boundary conditions

Taking advantage of the symmetry in geometry, loading and support conditions, one-half of the test specimen was modeled. The column bases were fixed against the three translations and three rotations (Figs. 9 and 10). The symmetry boundary conditions were assigned to the nodes on the symmetry plane. The Z-displacement at the top nodes of the middle column was controlled to match with the loading strategy followed in the experimental program (see Figs. 9 and 10).

## 5. Validation of FE models

The experimental results of the three tested specimens were used to validate the FE modeling techniques detailed previously in Sec. 4. The model validation is discussed below.

### 5.1. Mode of failure

Figs. 11–13, respectively, show the FE failure modes for test specimens: PC-C, MC-SMF, and PC-S. These figures present contours of maximum principal strain in concrete elements, contours of X-stress (for CFRP sheets), and damage contours – effective plastic strain – ranging from 0 to 1 (for concrete and CFRP sheets), with 0 indicating no damage and 1 designating full damage. The failure modes shown in these figures compare well with those observed in experiments, as shown earlier in Fig. 7. As expected, the beam ends of the control specimen PC-C had an obvious rotation, and the upper edge of the inner end of the beam was in contact with the center column. The crushing of concrete in the middle column connection zone caused the final failure of the test specimen (Fig. 11). The failure modes of specimen MC-SMF obtained from FE modeling (Fig. 12) also compare well with the experimental results (Fig. 7(b)). The flexural cracking of concrete in the tension zone and subsequent concrete crushing at the beam ends indicate the development of the plastic hinges observed in the test. As noted from the maximum principal strain contours shown in Fig. 13(a) for specimen PC-S, plastic hinge formation has been predicted for the strengthened beam near the middle joint due to the fracture of bottom NSM rebars and the rupture of horizontal CFRP sheets (see Fig. 13(b)) followed by concrete crushing at the top side of the beam. Also, at a later stage and as shown in Fig. 13(c), the FE predicted plastic hinge formation in the strengthened beam close to the outer columns, and it was due to the yielding of NSM steel rebars followed by interfacial end debonding of CFRP sheets (see Fig. 13(d)) and then the concrete crushing in the beam. The predicted end debonding of the CFRP sheets was almost the same as that observed in the experiment, as seen earlier in Fig. 7(c), which may validate the tiebreak contact parameters used for the FRP-to-concrete interface.

### 5.2. Load-displacement characteristics

The numerically obtained load–displacement envelopes for the middle column are compared with the experimental ones in Fig. 14. The two curves (numerical and experimental) for each test specimen are close to each other, and the peak load also matches very well. The numerical and experimental results of the load–displacement response are summarized in Table 2. The error in the prediction of peak load varies from 0% to 4%. Yet, the errors in the prediction of center column displacement at peak load, center column displacement at ultimate state, and energy dissipation at the ultimate state are 1%−17%, 6%−20%, and 3%−10%, respectively. As depicted in Fig. 14, the numerically obtained stiffness of the test specimens compares well with the experiments. Fig. 14 clearly
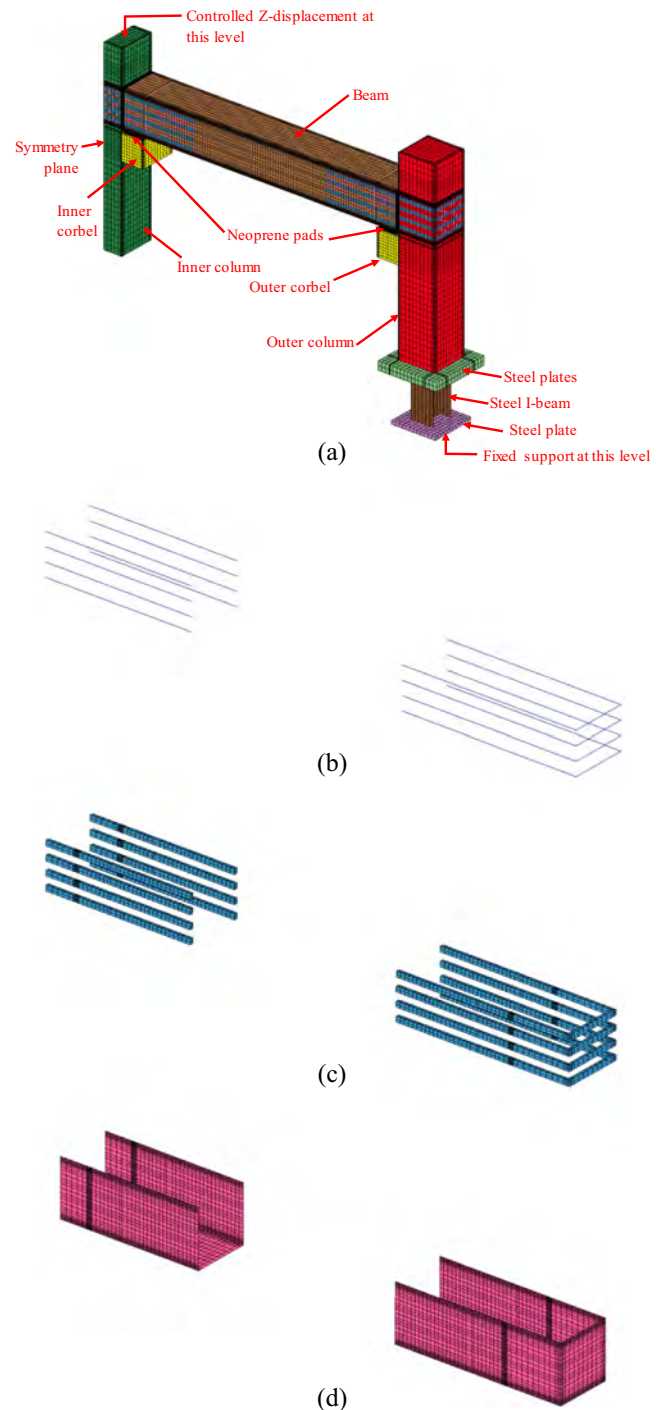


(a)

(b)

(c)

(d)

**Fig. 10.** FE model for one-half of specimen PC-S: (a) All parts; (b) NSM steel rebars; (c) Epoxy adhesive mortar; (d) FRP sheets.

illustrates that the numerical models simulated the softening behavior very effectively, which verifies the precision of the constitutive models used in this work. The FE analysis showed that compared with the monolithic specimen MC-SMF, the precast control specimen PC-C had a very high risk of progressive collapse. The FE analysis confirmed the significant peak load enhancement provided by the innovative NSM/FRP strengthening technique of specimen PC-S, for which the predicted peak load was about 17 times that of specimen PC-C and almost the same as that of specimen MC-SMF. The numerically predicted energy dissipation in specimen PC-S was substantially higher than the control one (~11
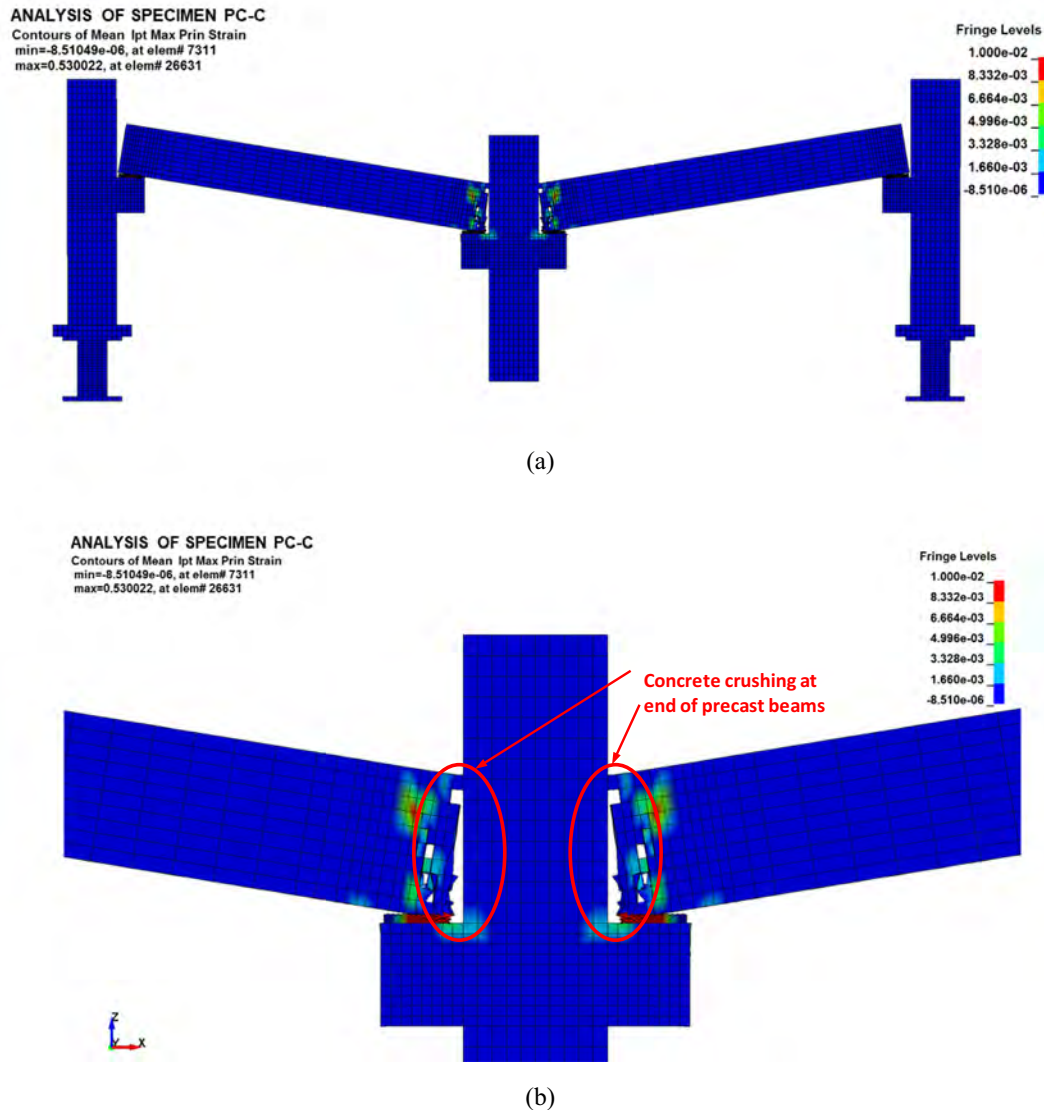
(a)



(b)

**Fig. 11.** FE mode of failure for specimen PC-C: (a) Whole specimen; (b) Middle joint.

times). Yet, numerically predicted energy dissipation and displacement ductility ratio in specimen PC-S were about 45% and 30%, respectively, of the monolithic specimen MC-SMF. This is because of the rupture of CFRP sheets followed by fracture of bottom NSM rebars, which resulted in significant loss of vertical load at a displacement level smaller than that of specimen MC-SMF.

*5.3. Strain gage analysis*

Figs. 15 and 16 illustrate the comparisons between the numerical and measured values of peak strains in steel rebars for specimens MC-SMF and PC-S, respectively. Table 2 presents numerical and experimental values of strains at peak load for bottom rebars of beams at the interior column face. For specimen PC-S, a comparison between experimental and FE strain at peak load for the bottom and top NSM steel rebars at the inner and outer column face, respectively, is illustrated in Table 2. In addition, for specimen PC-S, Table 2 enlists a comparison between experimental and FE strain at peak load for the bottom edge of horizontal CFRP sheets at the inner column face. The numerical results are in good conformity with experiments. The results of specimen MC-SMF, shown in Fig. 15 and Table 2, indicate yielding of bottom rebars of the beam

at the center column and top rebars at outer columns. It may be noted that the stress level in these rebars significantly exceeds the yield limit, which indicates the formation of plastic hinges at the beam ends, as previously discussed. However, the level of stress in the bottom beam rebars at the middle column in specimens PC-C and PC-S were low due to the discontinuity of these rebars (Table 2). For specimen PC-S and as shown in Table 2 and Fig. 16, large strains (significantly exceeding the yield strain) were both recorded and predicted at peak load for the extreme tension NSM steel rebars at inner and outer column faces, which confirms the development of plastic hinges in the strengthened portion of the beams near inner and outer columns, as discussed previously. As seen in Fig. 16(c), both experimental and FE strain curves revealed rupture of the bottom edge of horizontal CFRP sheets at the inner column face. However, at the outer column face, CFRP interfacial end debonding occurred, as presented in Fig. 16(d).

In order to aid in understanding the contribution of each strengthening part in enhancing the progressive collapse resistance of specimen PC-S, Table 3 was created. It lists the FE stresses in different strengthening parts at the critical section of the middle joint of strengthened specimen PC-S at peak load level. As seen from the table, three of the four side NSM rebars had tensile stres-
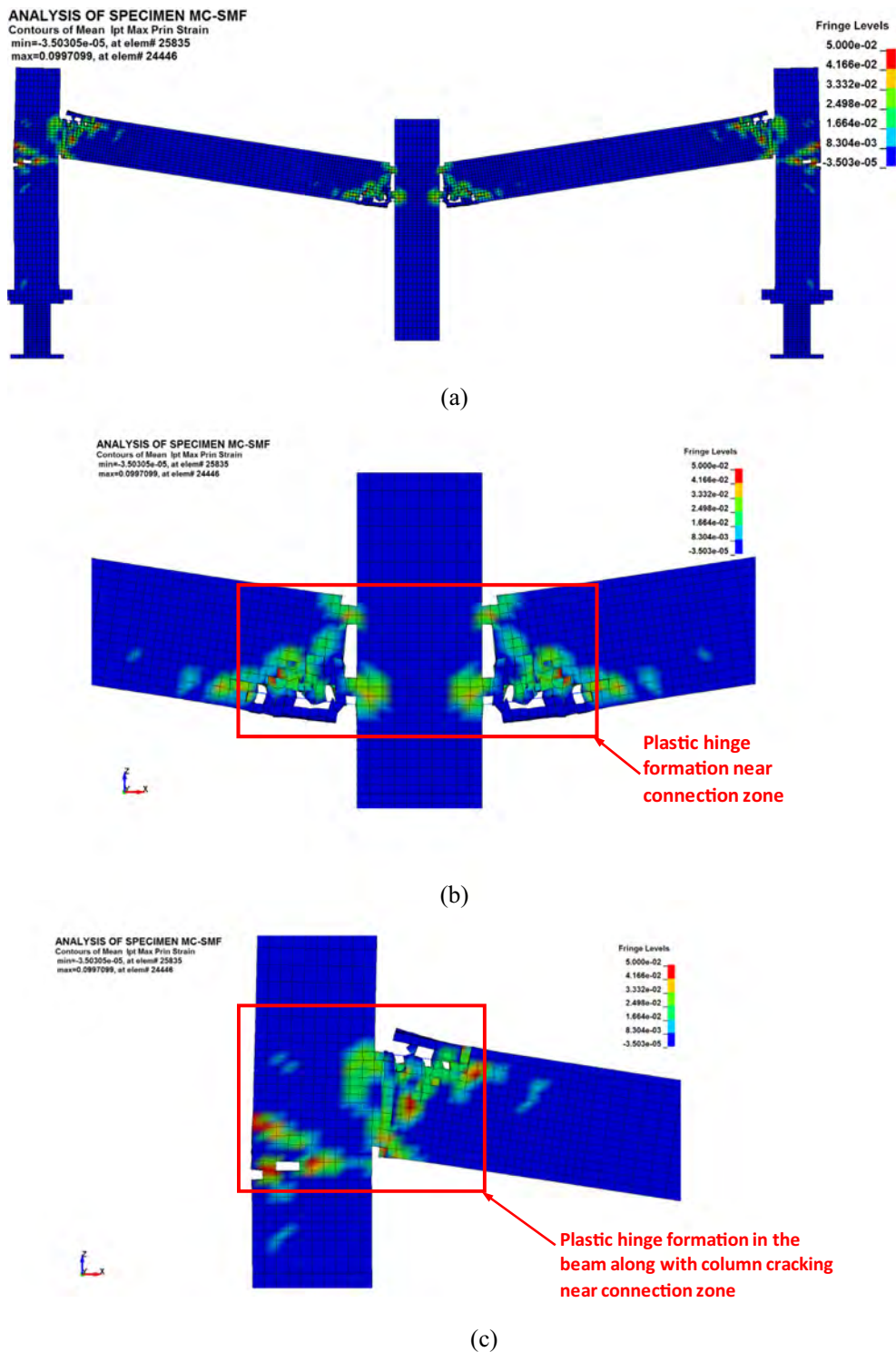
(a)



(b)



(c)

**Fig. 12.** FE mode of failure for specimen MC-SMF: (a) Whole specimen; (b) Middle joint; (c) End joint.

ses at peak load level, with the first two rebars from the bottom side (rebar 1 and rebar 2) going into the post-yield zone by having stresses of 1.02 times the yield stress. This reveals the contribution of NSM rebars in resisting the flexural capacity at the critical section. In addition, as presented in Table 3, tensile stresses in the extreme bottom edge of the horizontal CFRP layer (predicted at critical section) reached 98% of the ultimate tensile strength of the CFRP sheet. This indicated the full utilization of the horizontal CFRP layer in increasing the flexural resistance of the specimen at

the inner column face. Moreover, at maximum load, the peak stress in the vertical CFRP layer (in the Z-direction) was predicted at mid-depth of the beam section close to the inner column face, with a value of about 69% of the effective tensile stress in the CFRP layer at ultimate shear strength (calculated as per ACI 440.2R-17 [46]). This indicates that as per the intended design, the full shear strength capacity of the strengthened beam section was not reached owing to flexural failure at the critical section. As per ACI 440.2R-17 [46], this predicted stress (=183 MPa) corresponded
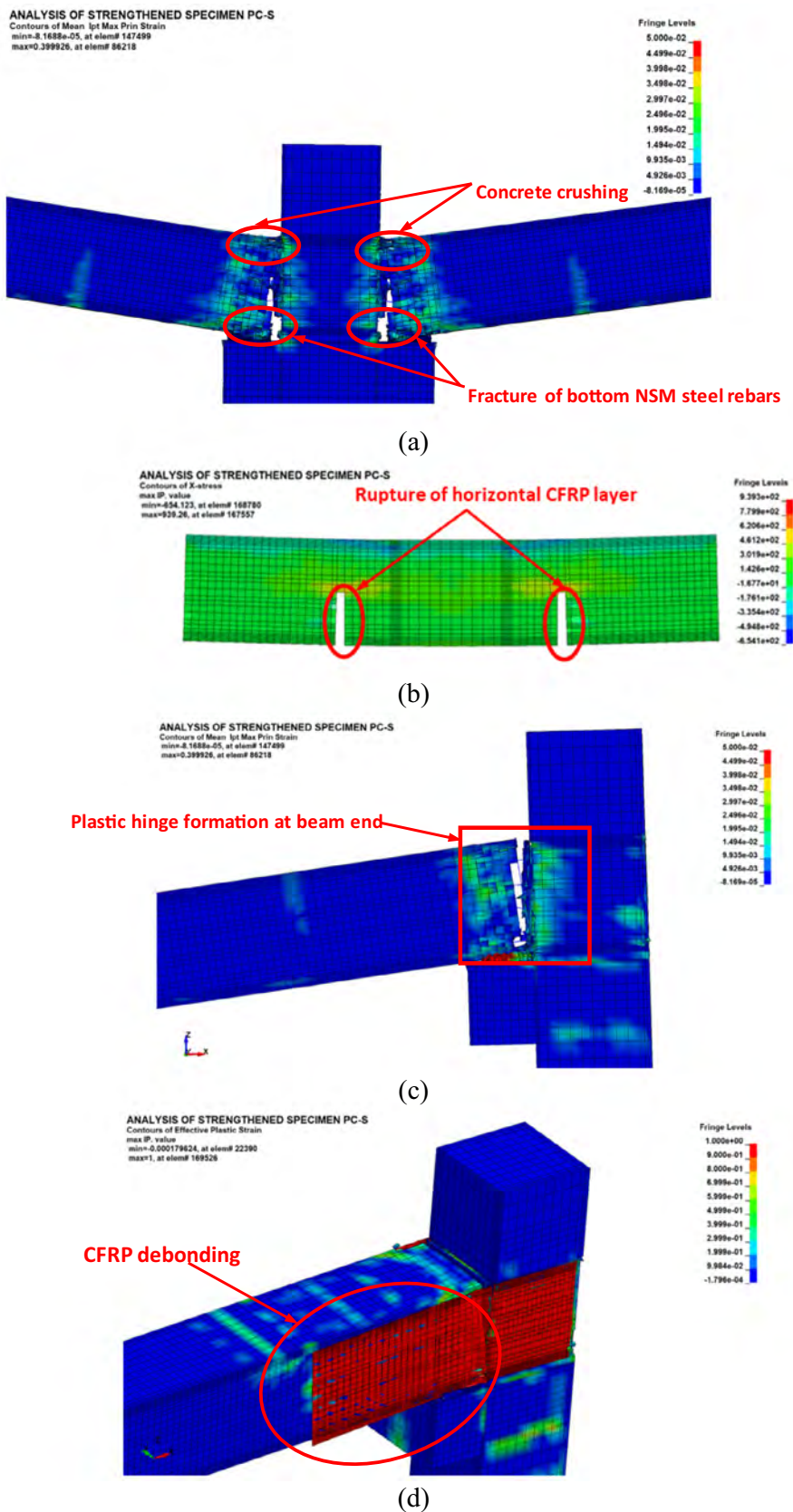
(a)



(b)



(c)



(d)

**Fig. 13.** FE mode of failure for specimen PC-S: (a) Middle joint; (b) FRP sheets at middle joint; (c) End joint; (d) FRP sheets at end joint.
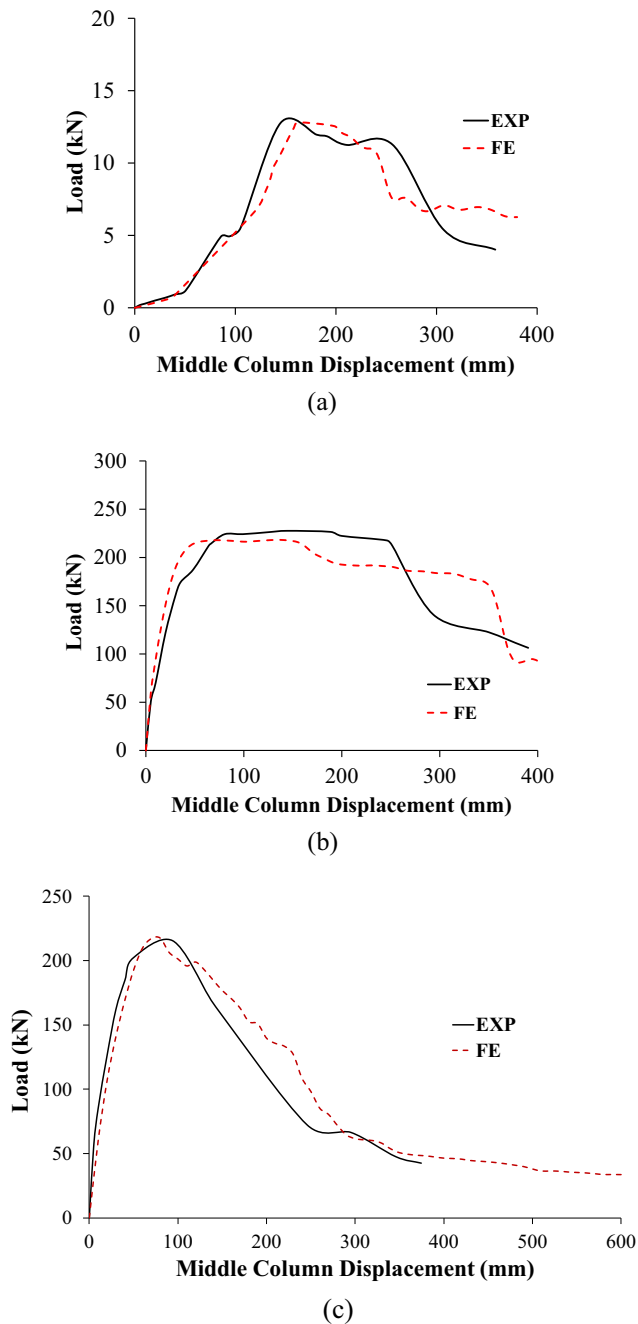
(a)



(b)



(c)

**Fig. 14.** Comparison of experimental and FE load-displacement envelopes for: (a) Specimen PC-C; (b) Specimen MC-SMF; (c) Specimen PC-S.



(a)



(b)



(c)

**Fig. 15.** Comparison of experimental and FE load vs. rebar strain curves for specimen MC-SMF: (a) Bottom rebars of beam at face of inner column; (b) Top rebars of beam at face of outer column; (c) Outer rebars of exterior column near connection zone.

to shear strength enhancement provided by the vertical CFRP layer of $V_f$ = 108 kN. Since beams of test specimens had large displacement combined with significant damage (wide flexure cracking and concrete crushing in the compression zone), the contribution of concrete to the shear strength of the strengthened beam portion could be neglected [26]. The shear capacity was then assumed as $V_u = V_f$ = 108 kN. The ultimate load of the test specimen corresponding to the predicted value of stress in the vertical CFRP layer = 2 × 108 = 216 kN, which is almost the same as the numerically predicted peak load of specimen PC-S (=217 kN). In conclusion, predicted stresses in the different parts of the strengthening system (NSM rebars as well as horizontal and vertical CFRP layers) revealed that each part contributed efficiently in enhancing the progressive collapse resistance of specimen PC-S as per the intended purpose.
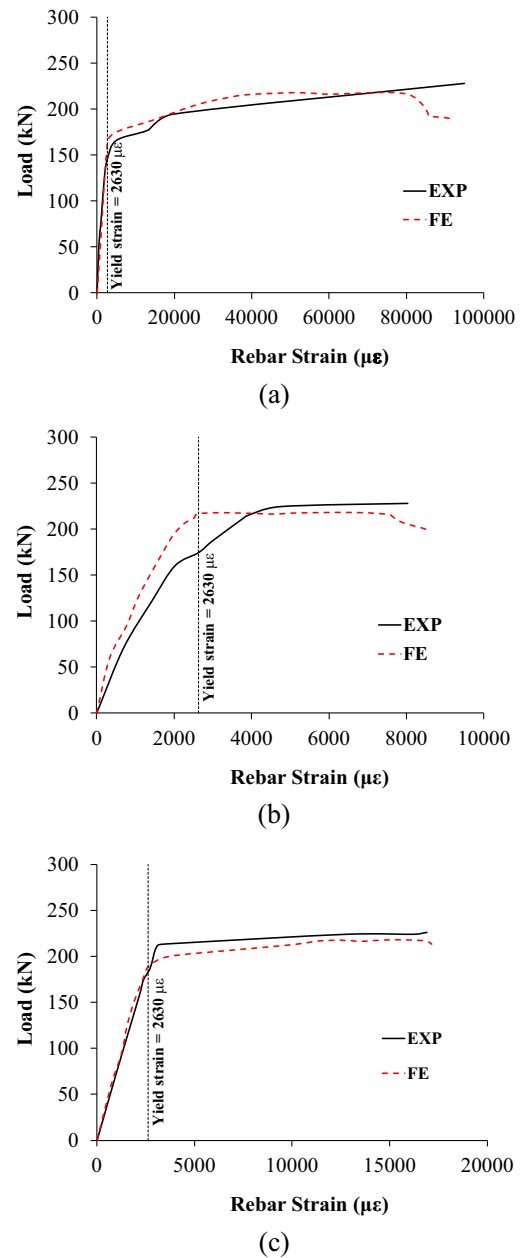
## 6. Parametric study

### 6.1. Effect of end anchorage of CFRP sheets at outer joints

As discussed earlier, the interfacial end debonding for CFRP sheets at the outer joints of specimen PC-S could have been alleviated by the provision of proper end anchorage through: full FRP wrapping (if possible), mechanical fasteners, fiber anchors, or bolted steel plates at CFRP ends. The effect of providing bolted steel plates at the end of CFRP sheets of the outer beam-column connections was studied numerically. In this regard, another strengthened specimen called "PC-S-EA" was modeled. This specimen was exactly the same as PC-S except that the CFRP sheets at outer connections were extended by 100 mm – to avoid anchoring in the NSM area – and then anchored using two ASTM A36 steel plates
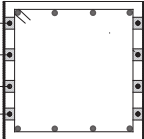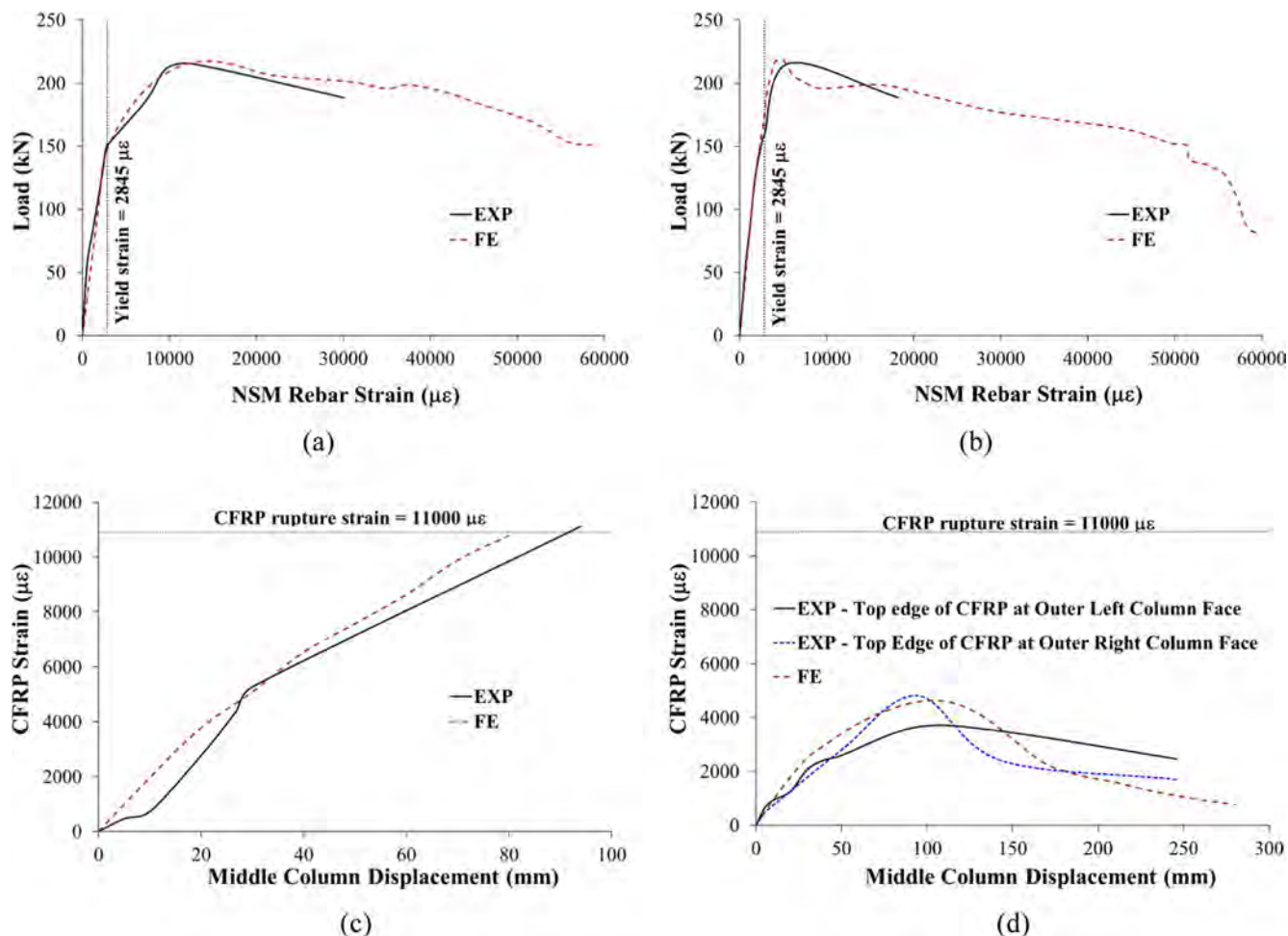
**Fig. 16.** Comparison of experimental and FE strain curves for specimen PC-S: (a) Bottom NSM rebar at face of inner column; (b) Top NSM rebar at face of outer column; (c) Bottom edge of horizontal CFRP sheets at inner column face; (d) Top edge of horizontal CFRP sheets at outer column face.

**Table 3**
FE stresses in different strengthening parts at peak load of strengthened specimen PC-S*

| Strengthening part | | Location | Stress component | Stress value (MPa)**, † |
|---|---|---|---|---|
| NSM steel rebars |  | Rebar 1 | Axial stress | 582 (=1.02$f_y$) |
| | | Rebar 2 | | 579 (=1.02$f_y$) |
| | | Rebar 3 | | 362 (=0.64$f_y$) |
| | | Rebar 4 | | −112 (=−0.2$f_y$) |
| Horizontal CFRP layer | | Extreme bottom edge | Stress in X-direction | 1033 (=0.98$f_{fu}$) |
| | | Extreme top edge | | −348 |
| Vertical CFRP layer | | Mid-depth of beam section | Stress in Z-direction | 183 (=0.69$f_{fe}$) |

* Stresses were predicted at critical section of middle beam-column connection.
** Positive value means tensile stress and negative value means compressive stress.
† $f_y$ = yield strength of NSM steel rebars; $f_{fu}$ = ultimate tensile strength of CFRP sheet; $f_{fe}$ = effective tensile stress in the CFRP shear reinforcement (vertical CFRP layer) at ultimate shear strength, as calculated from ACI 440.2R-17 [46].

with dimensions of 350 × 100 × 5 mm. These plates were connected via 4 φ10 mm high strength threaded rods at a center-to-center spacing of 80 mm, as seen in Fig. 17(a). As seen in Fig. 17 (b), steel plates were modeled using eight-node solid elements, whereas two-node beam elements were used to represent threaded rods. The perfect bond was assumed between the steel plates and the CFRP sheets. The FE output results of specimen PC-S-EA are illustrated in Table 4 and Fig. 18. The failure mode at the inner joint was the same as that described for specimen PC-S, and it was thus not shown in Fig. 18. However, the mode of failure of the CFRP sheets at the outer joints changed from interfacial end debonding at a predicted CFRP strain of about 4620 με to debonding mode at a predicted CFRP strain of about 6800 με (see Table 4 and Fig. 18(c)). This debonding mode is commonly found in RC
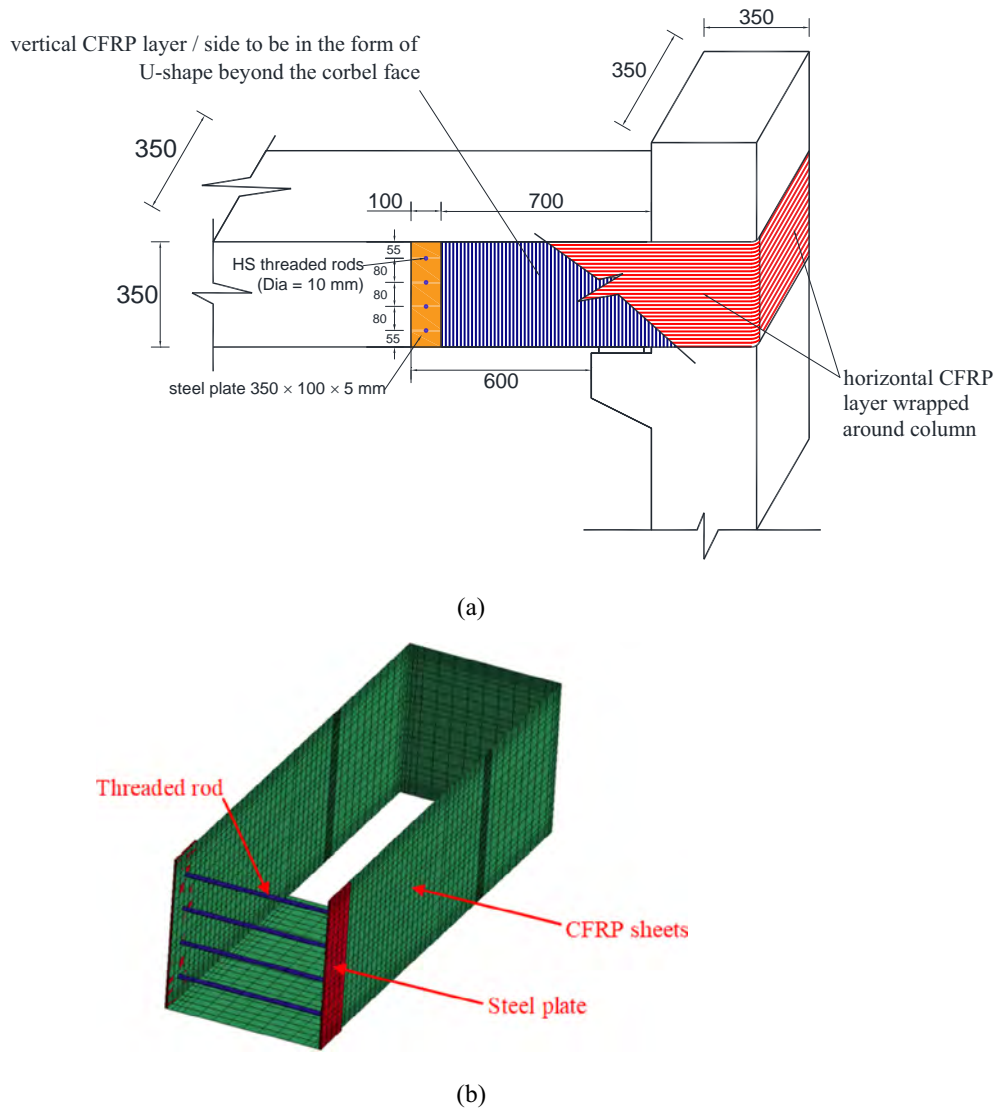
(a)



(b)

**Fig. 17.** Anchorage details for outer joint zone of strengthened specimen PC-S-EA: (a) Strengthening details (All dimensions are in mm); (b) FE model of anchorage system.

beams and slabs tested in flexure and having FRP sheets externally bonded to the tension side – known as intermediate crack (IC) debonding [47,62,63] as seen in Fig. 18(a). As depicted in Fig. 18 (b) and Table 4, the provision of end anchorage at the end of CFRP sheets of outer joints enhanced the peak load resistance by about 10% due to the delay of the CFRP debonding at the outer joints.

### 6.2. Effect of strengthening parameters

The FE modeling presented in Sec. 4 was also extended to investigate the impact of different strengthening parameters on the performance of upgraded specimens. In addition to specimens PC-S and PC-S-EA, the matrix for parametric analysis consisted of 34 specimens with different strengthening parameters such as the area of NSM reinforcement and the thickness of CFRP sheets (see Table 4). Six different NSM reinforcement areas ranging from 4 $\phi$6 mm per side to 4 $\phi$16 mm per side were studied. However, for CFRP sheets, six different thicknesses varying from 1 to 6 mm were investigated, in addition to the case of no FRP sheets, as illustrated in Table 4. It is worth to note here that in all specimens employed in the parametric study (except for the case of no FRP), the end CFRP sheets at outer connections were anchored using

bolted steel plates, which were the same as those used for specimen PC-S-EA (see Fig. 17). It should also be noted that in the analysis of specimens listed in Table 4, the material properties of specimen PC-S were utilized. It is observed from Table 4 that the thickness of transverse CFRP U-wraps was kept the same as the thickness of longitudinal CFRP sheets. As mentioned previously, the area of the transverse CFRP U-wraps was about 32% of that required by Eq. (14.1.2) of the ACI 440.2R-17 [46], which, as per both Almusallam et al. [47] and the test results of specimen PC-S, was found enough to inhibit the unwanted debonding modes such as the delamination of concrete cover and interfacial end debonding.

The numerical analysis results of the 34 specimens employed in this parametric study are summarized in Table 4. FE modes of failure for representative strengthened specimens employed in the parametric study are displayed in Fig. 19. For specimens without FRP sheets, tension-controlled flexural failure was anticipated in the beams at both inner and outer joints due to steel yielding followed later by crushing of concrete, as shown in Fig. 19(a) for specimen PC-S-No-FRP-D6. For all 6 specimens with one layer of CFRP sheets, failure was similar to specimen PC-S-EA (same as specimen PC-S-EA-1L-D12 in Table 4), and it was in the following order: steel

**Table 4**
Details and FE results of specimens used in the parametric study*

| Specimen ID | Hybrid strengthening scheme | | FE results | | | | | | | | | | | |
|---|---|---|---|---|---|---|---|---|---|---|---|---|---|---|
| | NSM strengthening / side | No. of CFRP layers / side ($n_h = n_v$) | $P_u$ (kN) | $\Delta_{u,c}$(mm) | $P_y$ (kN) | $\Delta_y$(mm) | $\Delta_u$(mm) | $\mu_\Delta$ | $E_u$ (kN.m) | $\varepsilon_{NSM,bot}$(με) | $\varepsilon_{NSM,top}$(με) | $\varepsilon_{FRP,bot}$(με) | $\varepsilon_{FRP,top}$(με) | Failure mode of middle joint |
| PC-S | 4 φ12 mm | 1 | 217 | 80 | 146 | 32 | 154 | 5 | 29 | 13,184 | 5071 | 10,785 | 4623 | SY-FR-CC |
| PC-S-EA | 4 φ12 mm | 1 | 240 | 90 | 146 | 32 | 130 | 4 | 32 | 19,676 | 24,827 | 10,952 | 6795 | SY-FR-CC |
| PC-S-No-FRP-D6 | 4 φ6 mm | 0 | 72 | 130 | 27 | 10 | 164 | 16 | 10 | 103,929 | 133,852 | – | – | SY-CC |
| PC-S-No-FRP-D8 | 4 φ8 mm | 0 | 102 | 150 | 41 | 11 | 231 | 21 | 21 | 91,505 | 104,197 | – | – | SY-CC |
| PC-S-No-FRP-D10 | 4 φ10 mm | 0 | 134 | 170 | 87 | 20 | 291 | 15 | 35 | 81,613 | 83,702 | – | – | SY-CC |
| PC-S-No-FRP-D12 | 4 φ12 mm | 0 | 172 | 140 | 102 | 22 | 288 | 13 | 43 | 61,447 | 60,710 | – | – | SY-CC |
| PC-S-No-FRP-D14 | 4 φ14 mm | 0 | 210 | 150 | 135 | 31 | 281 | 9 | 52 | 56,443 | 46,014 | – | – | SY-CC |
| PC-S-No-FRP-D16 | 4 φ16 mm | 0 | 250 | 150 | 171 | 40 | 245 | 6 | 53 | 22,879 | 32,484 | – | – | SY-CC |
| PC-S-EA-1L-D6 | 4 φ6 mm | 1 | 136 | 80 | 60 | 12 | 80 | 7 | 9 | 46,718 | 55,139 | 10,678 | 6428 | SY-FR-CC |
| PC-S-EA-1L-D8 | 4 φ8 mm | 1 | 150 | 70 | 98 | 21 | 81 | 4 | 10 | 42,785 | 42,916 | 10,207 | 6426 | SY-FR-CC |
| PC-S-EA-1L-D10 | 4 φ10 mm | 1 | 185 | 70 | 118 | 26 | 83 | 3 | 12 | 20,458 | 24,391 | 10,642 | 5980 | SY-FR-CC |
| PC-S-EA-1L-D12[†] | 4 φ12 mm | 1 | 240 | 90 | 146 | 32 | 130 | 4 | 32 | 19,531 | 24,827 | 10,952 | 6795 | SY-FR-CC |
| PC-S-EA-1L-D14 | 4 φ14 mm | 1 | 266 | 90 | 182 | 40 | 195 | 5 | 41 | 13,991 | 12,481 | 10,529 | 6755 | SY-FR-CC |
| PC-S-EA-1L-D16 | 4 φ16 mm | 1 | 307 | 110 | 209 | 44 | 223 | 5 | 55 | 9809 | 8328 | 10,771 | 5950 | SY-FR-CC |
| PC-S-EA-2L-D6 | 4 φ6 mm | 2 | 143 | 60 | 106 | 20 | 69 | 3 | 9 | 22,215 | 55,157 | 6038 | 6469 | SY-DB-CC |
| PC-S-EA-2L-D8 | 4 φ8 mm | 2 | 167 | 60 | 129 | 27 | 76 | 3 | 11 | 20,458 | 35,596 | 6533 | 6765 | SY-DB-CC |
| PC-S-EA-2L-D10 | 4 φ10 mm | 2 | 214 | 80 | 151 | 32 | 93 | 3 | 16 | 15,392 | 39,628 | 7187 | 8110 | SY-DB-CC |
| PC-S-EA-2L-D12 | 4 φ12 mm | 2 | 251 | 90 | 186 | 40 | 106 | 3 | 20 | 9901 | 26,419 | 7513 | 6693 | SY-DB-CC |
| PC-S-EA-2L-D14 | 4 φ14 mm | 2 | 281 | 90 | 209 | 44 | 170 | 4 | 41 | 7622 | 15,731 | 7780 | 4638 | SY-DB-CC |
| PC-S-EA-2L-D16 | 4 φ16 mm | 2 | 327 | 110 | 241 | 51 | 155 | 3 | 44 | 6431 | 14,818 | 7531 | 5097 | SY-DB-CC |
| PC-S-EA-3L-D6 | 4 φ6 mm | 3 | 172 | 60 | 119 | 22 | 65 | 3 | 8 | 19,720 | 43,816 | 5181 | 7075 | SY-DB-CC |
| PC-S-EA-3L-D8 | 4 φ8 mm | 3 | 186 | 60 | 151 | 31 | 91 | 3 | 14 | 16,870 | 36,526 | 5334 | 7476 | SY-DB-CC |
| PC-S-EA-3L-D10 | 4 φ10 mm | 3 | 230 | 70 | 182 | 36 | 77 | 2 | 16 | 11,857 | 29,601 | 5578 | 7690 | SY-DB-CC |
| PC-S-EA-3L-D12 | 4 φ12 mm | 3 | 269 | 80 | 206 | 42 | 99 | 2 | 19 | 7769 | 25,637 | 5670 | 5759 | SY-DB-CC |
| PC-S-EA-3L-D14 | 4 φ14 mm | 3 | 306 | 90 | 240 | 50 | 99 | 2 | 23 | 6909 | 19,309 | 5950 | 5194 | SY-DB-CC |
| PC-S-EA-3L-D16 | 4 φ16 mm | 3 | 338 | 110 | 261 | 55 | 125 | 2 | 34 | 6011 | 15,366 | 6171 | 4203 | SY-DB-CC |
| PC-S-EA-4L-D6 | 4 φ6 mm | 4 | 192 | 60 | 135 | 31 | 70 | 2 | 9 | 14,407 | 44,532 | 4525 | 4318 | SY-DB-CC |
| PC-S-EA-4L-D8 | 4 φ8 mm | 4 | 219 | 60 | 168 | 36 | 72 | 2 | 12 | 10,614 | 53,299 | 4783 | 3635 | SY-DB-CC |
| PC-S-EA-4L-D10 | 4 φ10 mm | 4 | 231 | 70 | 207 | 42 | 75 | 2 | 15 | 8058 | 26,275 | 4816 | 3007 | SY-DB-CC |
| PC-S-EA-4L-D12 | 4 φ12 mm | 4 | 282 | 80 | 224 | 50 | 84 | 2 | 17 | 7240 | 23,770 | 4736 | 5154 | SY-DB-CC |
| PC-S-EA-4L-D14 | 4 φ14 mm | 4 | 301 | 100 | 263 | 54 | 106 | 2 | 24 | 6209 | 27,051 | 5337 | 4456 | SY-DB-CC |
| PC-S-EA-4L-D16 | 4 φ16 mm | 4 | 340 | 110 | 283 | 63 | 130 | 2 | 35 | 4080 | 14,992 | 5210 | 3387 | SY-DB-CC |
| PC-S-EA-5L-D6 | 4 φ6 mm | 5 | 171 | 60 | 157 | 32 | 66 | 2 | 9 | 13,514 | 86,701 | 3874 | 4108 | SY-DB-CC |
| PC-S-EA-5L-D16 | 4 φ16 mm | 5 | 332 | 90 | 305 | 69 | 140 | 2 | 37 | 3832 | 9687 | 4483 | 3812 | SY-DB-CC |
| PC-S-EA-6L-D6 | 4 φ6 mm | 6 | 194 | 70 | 151 | 42 | 75 | 2 | 11 | 7657 | 63,445 | 3945 | 3125 | SY-DB-CC |
| PC-S-EA-6L-D16 | 4 φ16 mm | 6 | 327 | 80 | NY | NY | 140 | – | 37 | 2787 | 5604 | 3977 | 2561 | DB-CC |

* $n_h$ = No. of horizontal CFRP layers per side within connection region; $n_v$ = No. of vertical CFRP layers per side within connection region; $P_u$ = peak load; $\Delta_{u,c}$= middle column displacement at peak load; $P_y$ &$\Delta_y$ = load and middle column displacement at first yielding of bottom NSM rebars at inner column face; $\Delta_u$= middle column displacement at ultimate state; $\mu_\Delta$= displacement ductility = $\Delta_u/\Delta_y$; $E_u$ = energy dissipated at ultimate state, $\varepsilon_{NSM,bot}$ = strain at peak load for bottom NSM steel rebars at inner column face; $\varepsilon_{NSM,top}$ = strain at peak load for top NSM steel rebars at outer column face; $\varepsilon_{FRP,bot}$ = strain at peak load for bottom edge of horizontal CFRP sheets at inner column face; $\varepsilon_{FRP,top}$ = strain at peak load for top edge of horizontal CFRP sheets at outer column face; NY = No steel yielding; SY-FR-CC = flexural failure of strengthened portion of beam at inner column face due yielding of NSM rebars followed by rupture of horizontal CFRP layers and then crushing of concrete in the compression zone of beam; SY-CC = flexural failure of beam at inner column face due yielding of NSM rebars followed by crushing of concrete in the compression zone of beam; SY-DB-CC = flexural failure of strengthened portion of beam at inner column face due yielding of NSM rebars followed by intermediate crack debonding of horizontal CFRP layers and then crushing of concrete in the compression zone of beam; DB-CC = flexural failure of strengthened portion of beam at inner column face due to intermediate crack debonding of horizontal CFRP layers followed by crushing of concrete in the compression zone of beam.
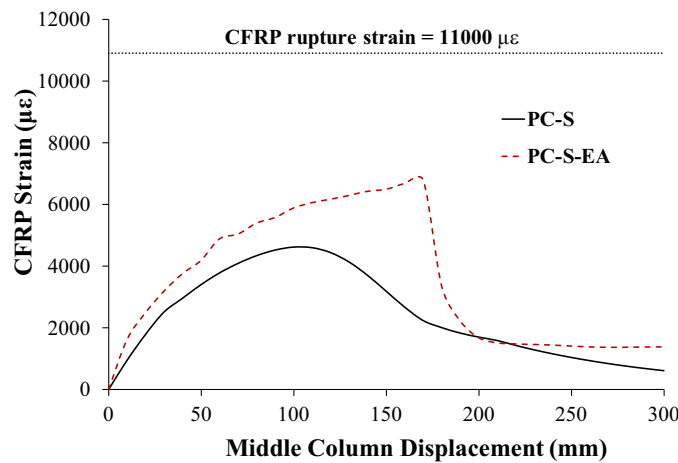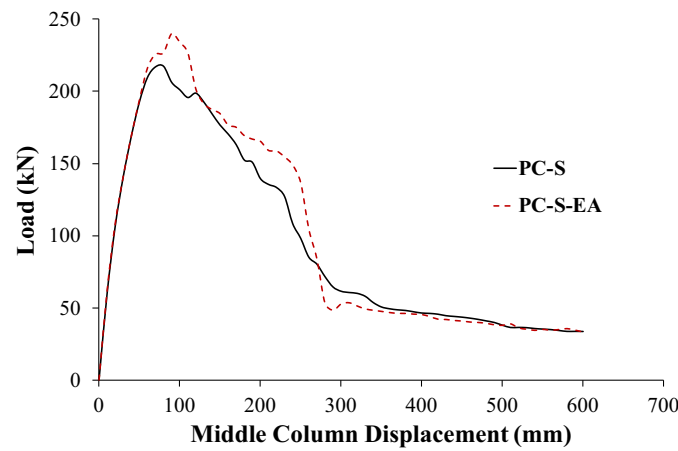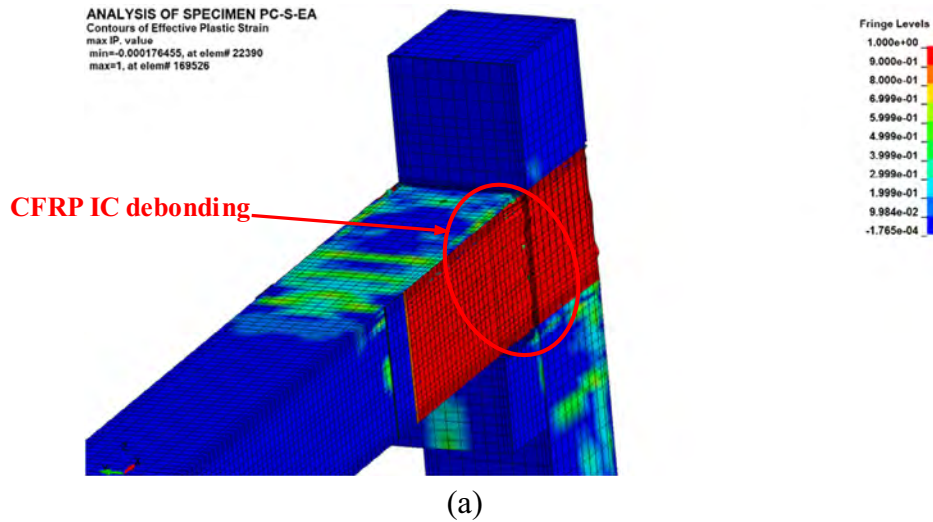↑ Same as specimen PC-S-EA.

(a)



(b)



(c)

**Fig. 18.** Effect of end anchorage on performance of specimen PC-S-EA (based on FE analysis): (a) Failure mode of CFRP sheets at outer joint; (b) Load-displacement curve in comparison with unanchored specimen PC-S; (c) Strain of top edge of horizontal CFRP sheets at outer column face in comparison with unanchored specimen PC-S.

yielding at the inner joint, steel yielding at outer joints, rupture of CFRP sheets at the inner joint, IC debonding of CFRP sheets at outer joints, crushing of concrete in beams at the inner joint, and finally crushing of concrete in beams at outer joints. However, for speci-

mens strengthened with two to five layers of CFRP sheets, failure was almost identical – an example is given in Fig. 19(b) for the inner joint of specimen PC-S-EA-4L-D12. It was in the following order: steel yielding at the inner joint, steel yielding at outer joints,
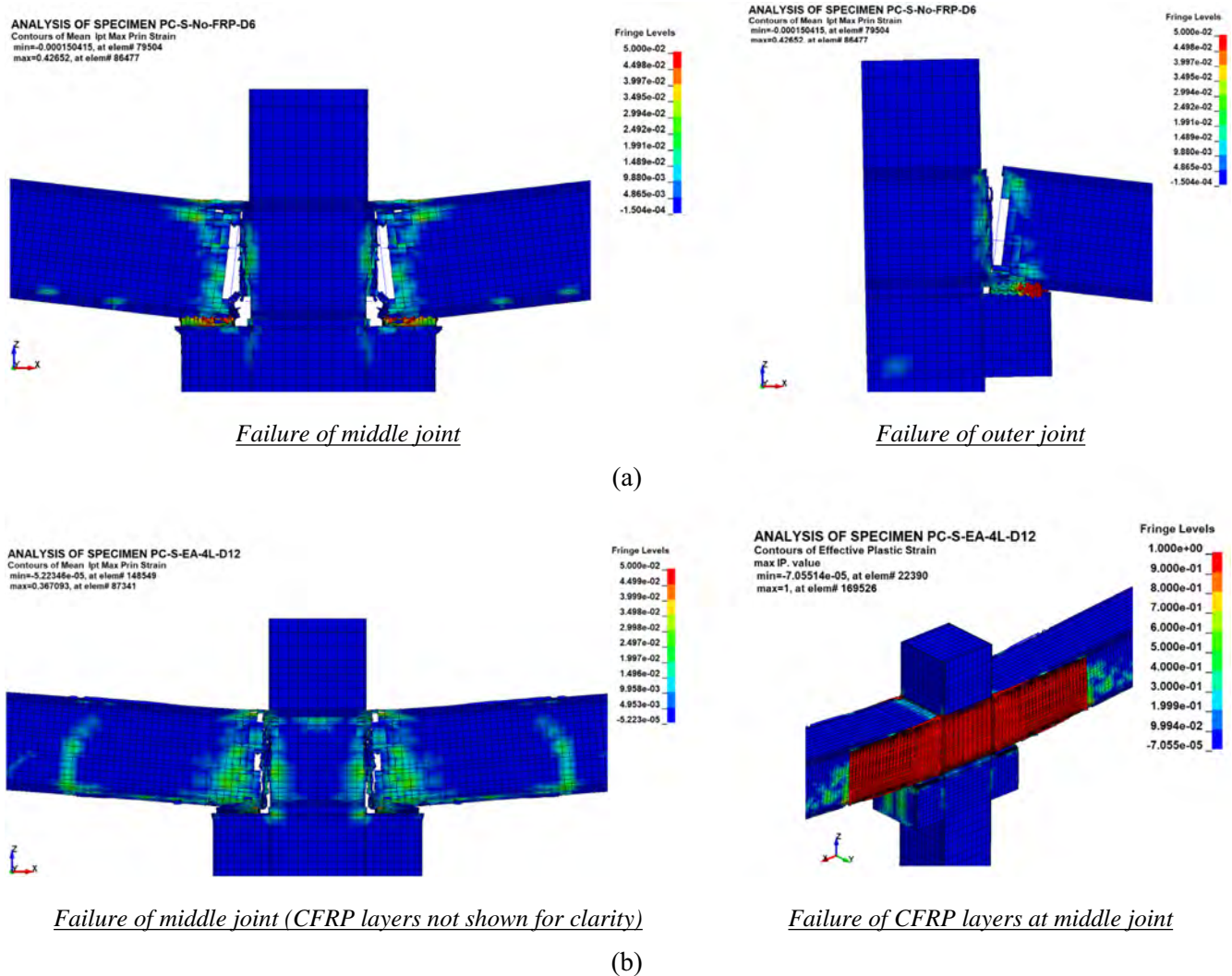
*Failure of middle joint*

*Failure of outer joint*

(a)



*Failure of middle joint (CFRP layers not shown for clarity)*

*Failure of CFRP layers at middle joint*

(b)

**Fig. 19.** FE mode of failure for representative strengthened specimens used in the parametric study: (a) Specimen PC-S-No-FRP-D6; (b) Specimen PC-S-EA-4L-D12.

IC debonding of CFRP sheets at the inner joint, IC debonding of CFRP sheets at outer joints, crushing of concrete in beams at the inner joint, and ultimately crushing of concrete in beams at outer joints. The same failure mode was predicted for specimen PC-S-EA-6L-D6, strengthened with 6 layers of CFRP sheets combined with 4 $\phi$6 mm NSM steel rebars per side. However, for specimen PC-S-EA-6L-D16, strengthened with 6 layers of CFRP sheets combined with 4 $\phi$16 mm NSM steel rebars per side, failure was different, as steel yielding was not predicted for the NSM rebars at the middle joint (strain at the peak load was 98% of the yield strain, as shown in Table 4). However, for the outer joints, the top NSM rebars reached a strain of about twice the yield strain at peak load, as depicted in Table 4. Load-displacement envelopes for representative samples of studied specimens are shown in Fig. 20. The influence of the number of CFRP layers on the load–displacement characteristics can be studied from Fig. 20. The enhancement in the number of CFRP layers from 1 to 4 did not have a significant effect on the pre-yield stiffness of the specimens. However, it has a considerable effect on the peak load resistance for specimens strengthened with a small area of NSM rebars as the peak load increased by about 42%, 46%, and 25% for $\phi$6, $\phi$8, and $\phi$10, respectively, when the number of CFRP layers increased from 1 to 4, as seen in Table 4 and Fig. 20. However, the number of CFRP layers has less effect on the enhancement in the peak load of specimens strengthened with a larger area of NSM rebars. The increase in

peak load was limited to 18%, 13%, and 11% for $\phi$12, $\phi$14, and $\phi$16 NSM rebars, respectively, when the number of CFRP layers increased from 1 to 4, as illustrated in Table 4 and Fig. 20.

As seen from Table 4, 22 specimens failed due to IC debonding of the bottom edge of horizontal CFRP sheets at the middle joint. For these 22 specimens, the debonding strain predicted by the FE analysis was compared with the debonding strain $\varepsilon_{fd}$ of the ACI 440.2R-17 [46] given by:

$$\varepsilon_{fd} = 0.41 \sqrt{\frac{f'_c}{n E_f t_f}} \quad (\text{Units} : \text{N, mm}) \tag{8}$$

where $f'_c$ = specified concrete strength; $n$ = number of plies of FRP reinforcement; $E_f$ = modulus of elasticity of FRP material; $t_f$ = thickness of one ply of FRP reinforcement. Fig. 21 shows this comparison. It is evident that the ACI equation underestimated the IC debonding strain of all specimens with an average ratio of 0.83 for the FRP strain predicted by the ACI model with respect to the strain predicted by the FE analysis. Thus, the equation of the ACI 440.2R-17 [46] can be used conservatively to anticipate the IC debonding strain at the bottom edge of horizontal FRP sheets at the middle joint of strengthened specimens.
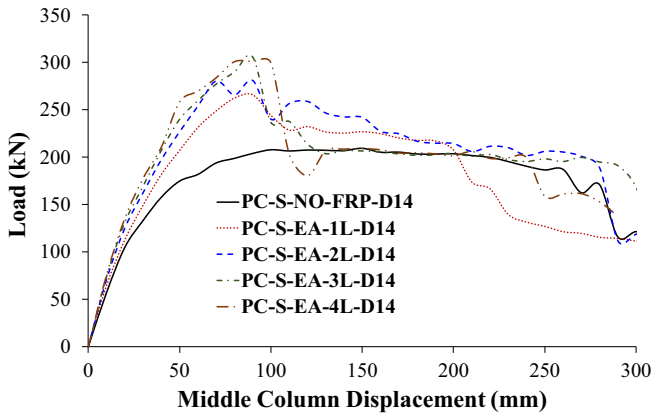
In order to help in assessing the effectiveness of the CFRP/NSM strengthening technique in enhancing the response of precast RC beam-column connections under column-loss scenario, a new
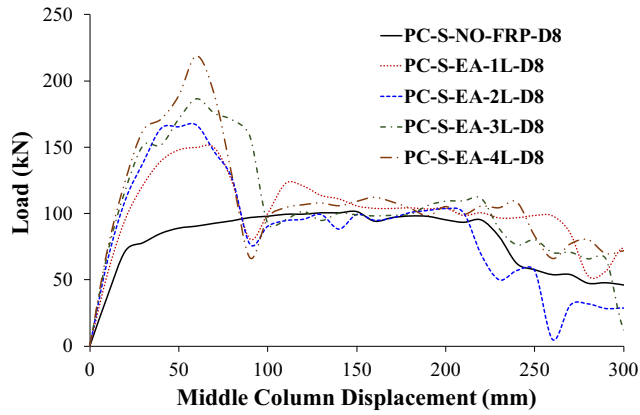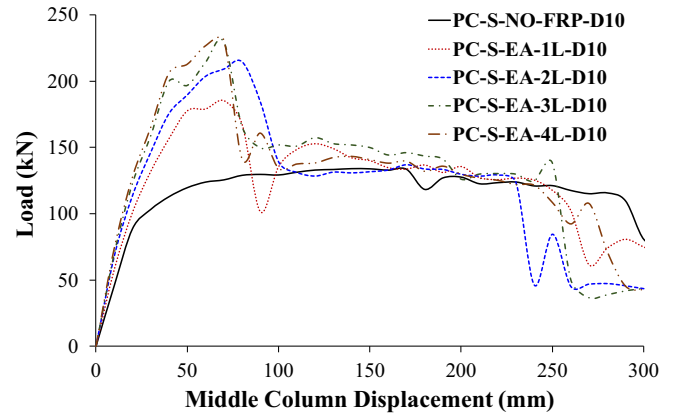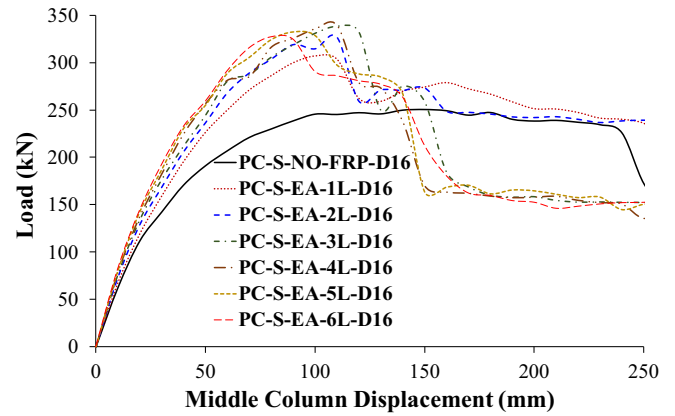
**Fig. 20.** Load-displacement envelopes for representative strengthened specimens used in the parametric study (based on FE analysis): (a) Specimens with 4 φ8 mm per side NSM rebars; (b) Specimens with 4 φ10 mm per side NSM rebars; (c) Specimens with 4 φ14 mm per side NSM rebars; (d) Specimens with 4 φ16 mm per side NSM rebars.

strengthening parameter ($\lambda_s$) was presented in this work. This parameter can be expressed as follows:

$$\lambda_s = \frac{M_{NSM} + M_{FRP}}{M_s} \tag{9}$$

where $M_{NSM}$ = moment capacity (at interior column face) of precast RC beam section strengthened by NSM steel rebars alone; $M_{FRP}$ = moment capacity (at interior column face) of precast RC beam section strengthened by horizontal FRP sheets alone; and $M_s$ = moment capacity (at interior column face) of beam section of the corresponding monolithic specimen having continuous longitudinal beam rebars (specimen MC-SMF). For simplicity, these moments can be estimated by assuming a reasonable value for the neutral axis depth of $c = 0.2h$; where $h$ = overall beam depth. The three moments can be then approximately assessed from

$$M_{NSM} = \sum_{i=1}^{n_{NSM}} A_{bi} f_{si} \left(d_{si} - \frac{\beta_1 c}{2}\right) \tag{10}$$

$$M_{FRP} = 0.4 n t_f \varepsilon_{fd} E_f h^2 \tag{11}$$

$$M_s = A_s f_y \left(d - \frac{\beta_1 c}{2}\right) \tag{12}$$

where $A_{bi}$ = area of single NSM rebar; $d_{si}$ = depth of $i^{th}$ NSM rebar; $f_{si}$ = stress in $i^{th}$ NSM rebar, given by

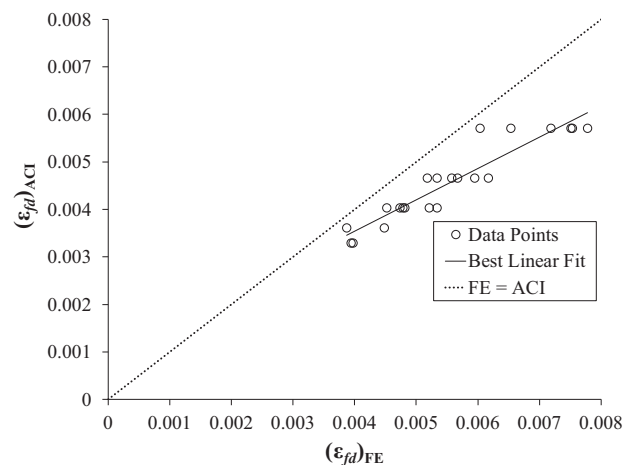$$f_{si} = \frac{0.003(d_{si} - c)}{c} E_s \leqslant f_{y,NSM} \tag{13}$$



**Fig. 21.** Comparison of IC debonding strain of bottom edge of horizontal CFRP sheets at middle joint of strengthened specimens predicted by ACI 440.2R-17 model with FE analysis.

where $f_{y,NSM}$ is the yield stress of NSM rebars and $E_s$ is the modulus of elasticity of steel rebars. The other parameters in the above equations are defined as: $\beta_1$ = factor relating depth of rectangular stress block, as provided by the ACI 318–19 code [40]; $\varepsilon_{fd}$= FRP debonding strain, as given by the ACI 440.2R-17 [46] (Eq. (8)); $A_s$ = area of tension beam reinforcement of monolithic specimen MC-SMF; $f_y$ = yield stress of tension rebars of monolithic specimen MC-SMF; $d$ = effective depth to the centroid of tension rebars of monolithic specimen MC-SMF. Another new parameter called "peak load efficiency ($\eta_p$)" was also developed in this study, and it is expressed as follows:

$$\eta_p = \frac{P_{u,precast}}{P_{u,monolithic}} \times 100\% \tag{14}$$

where $P_{u,precast}$ is the ultimate load of the strengthened specimen; $P_{u,monolithic}$ is the ultimate load of specimen MC-SMF having continuous longitudinal beam rebars. For the 34 specimens employed in this parametric study, the strengthening parameter was calculated and plotted versus the strain of bottom NSM rebars at the middle joint ($\varepsilon_{NSM,b}$), as shown in Fig. 22(a). The strain, shown in Fig. 22(a), was normalized by the tension control limit of 0.005 [40]. The regression analysis gives the following best-fit model:

$$\frac{\varepsilon_{NSM,b}}{0.005} = 24.66 e^{-2.15\lambda_s} \tag{15}$$

As depicted in Fig. 22(a), the strengthening parameter $\lambda_s$ should not exceed 1.49 in order to have a tension controlled beam section at the interior column face of the strengthened specimen.

Considering only the numerical results for the specimens having tension controlled beam section at interior beam-column interface (31 specimens), the strengthening parameter $\lambda_s$ was also plotted against the peak load efficiency ($\eta_p$), as presented in Fig. 22(b). It should be noted that the data point for $\lambda_s$ = 0 (taking the peak load of control unstrengthened specimen PC-C) was also added to the scatter plot of Fig. 22(b). The best-fit regression trendline has the following equation:

$$\eta_p = -17.74\lambda_s^2 + 121.15\lambda_s + 5.87 \tag{16}$$

The $R^2$ value for the above equation is 0.97 (for all 32 data points). From Fig. 22(b) and Eq. (14), it is clear that in designing of CFRP/NSM retrofitting scheme for the continuity at precast beam-column joints, the strengthening parameter $\lambda_s$ should not be less than 0.9 in order to achieve a 100% peak load efficiency. In conclusion, it is recommended to design the CFRP/NSM strengthening system with $0.9 \leq \lambda_s \leq 1.49$.

## 7. Conclusions

The main conclusions of this work can be briefly outlined as follows:

1. Although the ultimate load and energy dissipated in monolithic specimen MC-SMF having continuity of longitudinal beam rebars were substantially higher compared to existing precast specimen PC-C, the catenary action could not be developed because of: (i) insufficient restraint provided by the end columns, (ii) discontinuity of beams at the ends, (iii) discontinuity of columns due to the consideration of single story, and (iv) absence of column axial load.

2. The retrofitting of precast RC beam-column joints using the innovative CFRP/NSM technique significantly enhanced the load–displacement characteristics under column-loss scenario. The proposed technique was efficient at enhancing the peak load – representing the progressive collapse resistance in the flexural action phase – by about 16.9 times of the control precast specimen. However, the strengthened specimen had a peak load of about 95% of that of the monolithic specimen. Consequently, the suggested strengthening technique was successful at reducing the risk of progressive collapse of precast RC frames, especially at the flexural action phase. However, displacement ductility and energy dissipated at the ultimate state of the strengthened specimen were 51% and 53%, respectively, of those for the monolithic specimen. Therefore, in the post-flexural action phase, due to the brittle nature of FRP composites (low rupture strain), enhancement provided by this system is limited, as compared with the monolithic specimen.

3. Comparison of the FE and the experimental results demonstrates the relevance of the FE modeling for the estimation of the load–displacement response for existing precast, monolithic, and strengthened precast RC frames under column-loss scenarios. Good agreement was obtained between the experimental and FE results with prediction errors ranging from 0% to 4%, 1% to 17%, and 3% to 10% for peak load, center column displacement at peak load, and dissipated energy at ultimate state. This shows the appli-
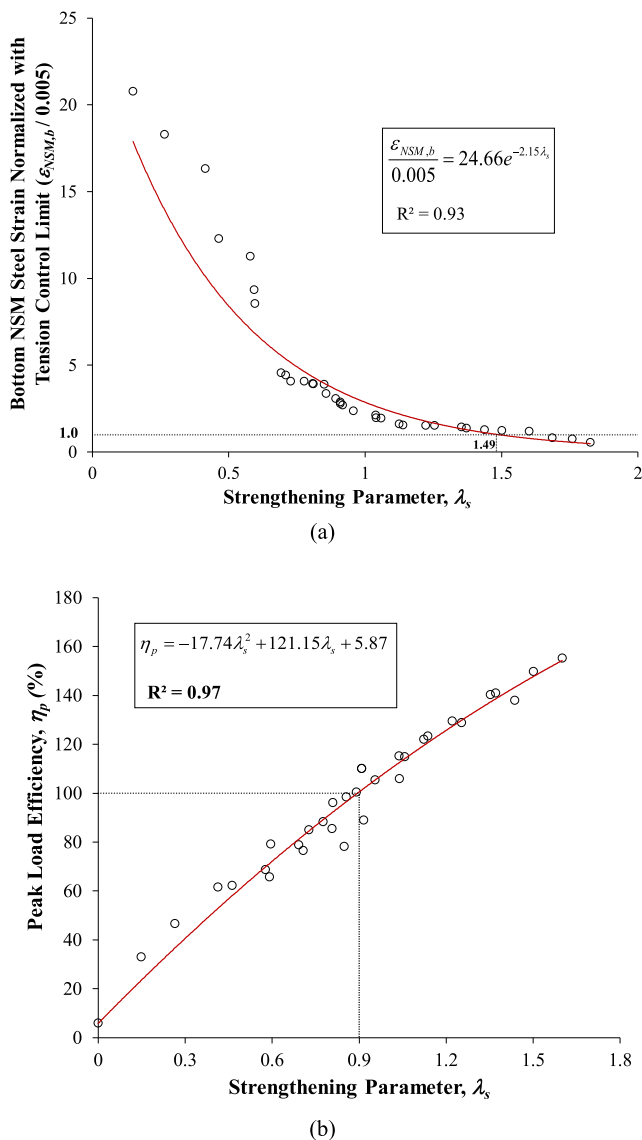


(a)



(b)

**Fig. 22.** Effect of strengthening parameter $\lambda_s$ on: (a) Strain of bottom NSM rebars at middle joint; (b) Peak load efficiency ($\eta_p$).

cability of the FE modeling procedures that may be employed in future research about the performance of precast RC beam-column joints for progressive collapse prevention.

4. The provision of end anchorage of bolted steel plates at the end of CFRP sheets of outer joints of strengthened specimen PC-S not only altered the failure mode from interfacial end debonding to IC debonding but also enhanced the peak load resistance by about 10% due to the delay of the CFRP debonding at outer joints.

5. It is recommended that the strengthening layers of the CFRP/NSM retrofitting system should cover the plastic hinge region, which can be achieved by extending the strengthening layers to at least twice the depth of the beam beyond the column face. This extension should not also be less than the tension development length of NSM rebars.

6. In this work, two parameters have been proposed: (i) strengthening parameter ($\lambda_s$) and (ii) peak load efficiency ($\eta_p$). These parameters were employed in comparing the behavior of strengthened precast RC beam-column joints under column-loss scenario with monolithic RC joint having continuous longitudinal beam rebars. In designing of strengthening scheme, the strengthening parameter $\lambda_s$ should not be less than 0.9 in order to achieve a 100% peak load efficiency. In order to ensure the tension-controlled flexural failure of the strengthened beam portion, it is recommended to design the CFRP/NSM strengthening system with $\lambda_s \leq 1.49$.

## CRediT authorship contribution statement

**Hussein M. Elsanadedy:** Conceptualization, Methodology, Writing - original draft. **Yousef A. Al-Salloum:** Supervision, Project administration, Funding acquisition. **Mohammed A. Alrubaidi:** Investigation, Validation, Writing - original draft. **Tarek H. Almusallam:** Visualization, Writing - review & editing. **Nadeem A. Siddiqui:** Visualization, Writing - review & editing. **Husain Abbas:** Writing - review & editing.

## Declaration of Competing Interest

The authors declare that they have no known competing financial interests or personal relationships that could have appeared to influence the work reported in this paper.

## Acknowledgements

## References

[1] E.V. Leyendecker, B.R. Ellingwood, Design methods for reducing the risk of progressive collapse in buildings, National Bureau of Standards, Washington, DC, 1977.

[2] McGuire W. Prevention of progressive collapse. Proc. Regional Conf. on Tall Buildings, Bangkok, Thailand.Choi HK, Choi YC, 1974.

[3] C.S. Choi, Development and testing of precast concrete beam-to-column connections, Eng. Struct. 56 (2013) 1820–1835.

[4] R. Vidjeapriya, K.P. Jaya, Experimental study on two simple mechanical precast beam column connections under reverse cyclic loading, J. Perform. Constr. Facil 27 (2013) 402–414.

[5] O. Ertas, S. Ozden, T. Ozturan, Ductile connections in precast concrete moment resisting frames, PCI J. 5 (2006) 2–12.

[6] M.K. Joshi, C.V. Murty, M.P. Jaisingh, Cyclic behaviour of precast RC connections, Indian Concr. J. 79 (2005) 43–50.

[7] H.M. Elsanadedy, T.H. Almusallam, Y.A. Al-Salloum, H. Abbas, Investigation of precast RC beam-column assemblies under column-loss scenario, Constr. Build. Mater. 142 (2017) 552–571.

[8] L.F. Maya, C. Zanuy, L. Albajar, C. Lopez, J. Portabella, Experimental assessment of connections for precast concrete frames using ultra high performance fibre reinforced concrete, Constr. Build. Mater. 48 (2013) 173–186.

[9] G. Magliulo, M. Ercolino, M. Cimmino, V. Capozzi, G. Manfredi, FEM analysis of the strength of RC beam-to-column dowel connections under monotonic actions, Constr. Build. Mater. 69 (2014) 271–284.

[10] D.E. Allen, W.R. Schriever, Progressive collapse, abnormal load, and building codes, structural failure: modes, causes, responsibilities, Proc. American Society of Civil Engineers, New York, USA, 1972.

[11] T.H. Almusallam, H.M. Elsanadedy, H. Abbas, S.H. Alsayed, Y.A. Al-Salloum, Progressive collapse analysis of a RC building subjected to blast loads, Int J Struct Eng Mech 36 (3) (2010) 301–319.

[12] T. Almusallam, Y. Al-Salloum, T. Ngo, P. Mendis, H. Abbas, Experimental investigation of progressive collapse potential of ordinary and special moment-resisting reinforced concrete frames, Mater. Struct. 50 (2017) 137.

[13] H.M. Elsanadedy, T.H. Almusallam, Y.R. Alharbi, Y.A. Al-Salloum, H. Abbas, Progressive collapse potential of a typical steel building due to blast attacks, J. Constr. Steel Res. 101 (2014) 143–157.

[14] J. Choi, D. Chang, Prevention of progressive collapse for building structures to member disappearance by accidental actions, J Loss Prevent Proc 22 (2009) 1016–1019.

[15] Y.A. Al-Salloum, T.H. Almusallam, M.Y. Khawaji, T. Ngo, H.M. Elsanadedy, H. Abbas, Progressive collapse analysis of RC buildings against internal blast, Adv. Struct. Eng. 18 (12) (2015) 2181–2192.

[16] P.X. Dat, T.K. Haiand, Y. Jun, A simplified approach to assess progressive collapse resistance of reinforced concrete framed structures, Eng. Struct. 101 (2015) 45–57.

[17] Y. Bao, S.K. Kunnath, S. El-Tawil, H.S. Lew, Macromodel-based simulation of progressive collapse: RC frame structures, J Struct Eng-ASCE 134 (7) (2008) 1079–1091.

[18] S.B. Kang, K.H. Tan, Behaviour of precast concrete beam-column sub-assemblies subject to column removal, Eng. Struct. 93 (2015) 85–96.

[19] S.M. Alcocer, J.O. Jirsa, Strength of reinforced concrete frame connections rehabilitated by jacketing, ACI Struct. J. 90 (3) (1993) 249–261.

[20] A. Ghobarah, T.S. Aziz, A. Biddah, Rehabilitation of reinforced concrete frame connections using corrugated steel jacketing, ACI Struct. J. 94 (3) (1997) 282–294.

[21] C. Antonopoulos, T.C. Triantafillou, Experimental investigation of FRP-strengthened RC beam-column joints, J Compos Constr, ASCE 7 (1) (2003) 39–49.

[22] Y.A. Al-Salloum, T.H. Almusallam, Seismic response of interior beam-column joints upgraded with FRP sheets, I: Experimental study, J Compos Constr, ASCE 11 (6) (2007) 575–589.

[23] S.H. Alsayed, Y.A. Al-Salloum, T.H. Almusallam, N.A. Siddiqui, Seismic response of FRP-upgraded exterior RC beam-column joints, J Compos Constr, ASCE 14 (2) (2010) 195–208.

[24] Y.A. Al-Salloum, N.A. Siddiqui, H.M. Elsanadedy, A.A. Abadel, M.A. Aqel, Textile-reinforced mortar versus FRP as strengthening material for seismically deficient RC beam-column joints, J. Compos. Constr, ASCE 15 (6) (2011) 920–933.

[25] Da Fonseca T, de Almeida SF, de Hanai JB. Beam-to-column connection of a precast concrete frame strengthened by NSM CFRP strips. In: Advances in FRP Composites in Civil Engineering, Editors: Ye L, Feng P, Yue Q, Springer, 2011, DOI: 10.1007/978-3-642-17487-2_189.

[26] Y.A. Al-Salloum, M.A. Alrubaidi, H.M. Elsanadedy, T.H. Almusallam, R.A. Iqbal, Strengthening of precast RC beam-column connections for progressive collapse mitigation using bolted steel plates, Eng. Struct. 161 (2018) 146–160.

[27] Pan J, Wang A, Wu F. Strengthening of precast RC frame to mitigate progressive collapse by externally bonded CFRP sheets anchored with HFRP anchors. Advances in Civil Engineering Volume 2018, Article ID 8098242, 11 pages.

[28] J. Esmaeili, N. Ahooghalandary, Introducing an easy-install precast concrete beam-to-column connection strengthened by steel box and peripheral plates, Eng. Struct. 205 (2020) 110006.

[29] H. Wang, E.M. Marino, P. Pan, Design, testing and finite element analysis of an improved precast prestressed beam-to-column joint, Eng. Struct. 199 (2019) 109661.

[30] Z.Y. Zhang, R. Ding, X. Nie, J.S. Fan, Seismic performance of a novel interior precast concrete beam-column joint using ultra-high performance concrete, Eng. Struct. 222 (2020) 111145.

[31] H. Wang, E.M. Marino, P. Pan, H. Liu, X. Nie, Experimental study of a novel precast prestressed reinforced concrete beam-to-column joint, Eng. Struct. 156 (2018) 68–81.

[32] P.K. Aninthaneni, R.P. Dhakal, J. Marshall, J. Bothara, Nonlinear cyclic behaviour of precast concrete frame sub-assemblies with "dry" end plate connection, Structures 14 (2018) 124–136.

[33] J. Zhang, C. Ding, X. Rong, H. Yang, K. Wang, B. Zhang, Experimental seismic study of precast hybrid SFC/RC beam–column connections with different connection details, Eng. Struct. 208 (2020) 110295.

[34] K. Qian, S.L. Liang, F. Fu, Q. Fang, Progressive collapse resistance of precast concrete beam-column sub-assemblages with high-performance dry connections, Eng. Struct. 198 (2019) 109552.

[35] Y. Zhou, X. Hu, Y. Pei, H.J. Hwang, T. Chen, W. Yi, L. Deng, Dynamic load test on progressive collapse resistance of fully assembled precast concrete frame structures, Eng. Struct. 214 (2020) 110675.

[36] K. Qian, S.L. Liang, X.Y. Xiong, F. Fu, Q. Fang, Quasi-static and dynamic behavior of precast concrete frames with high performance dry connections subjected to loss of a penultimate column scenario, Eng. Struct. 205 (2020) 110115.

[37] S.B. Kang, K.H. Tan, E.H. Yang, Progressive collapse resistance of precast beam–column sub-assemblages with engineered cementitious composites, Eng. Struct. 98 (2015) 186–200.

[38] Livermore Software Technology Corporation (LSTC). LS-DYNA user's keyword manual (nonlinear dynamic analysis of structures in three dimensions) Volume 1. Version 971, LSTC, Livermore, CA, 2007.

[39] T.H. Almusallam, H.M. Elsanadedy, Y.A. Al-Salloum, N.A. Siddiqui, R.A. Iqbal, Experimental investigation on vulnerability of precast RC beam-column joints to progressive collapse, KSCE J. Civil. Eng. 22 (10) (2018) 3995–4010.

[40] ACI Committee 318. Building code requirements for structural concrete and commentary. ACI 318-19, American Concrete Institute, Detroit, MI, USA, 2019.

[41] American Society for Testing and Materials (ASTM). Standard test method for compressive strength of cylindrical concrete specimens. ASTM C39/C39M, West Conshohocken, PA, USA, 2010.

[42] American Society for Testing and Materials (ASTM). Standard test method for compressive strength of hydraulic cement mortars (using 2-in. or [50-mm] cube specimens). ASTM C109/C109M, West Conshohocken, PA, USA, 2008.

[43] American Society for Testing and Materials (ASTM). Standard test methods for tension testing of metallic materials. ASTM E8/E8M, West Conshohocken, PA, USA, 2009.

[44] American Society for Testing and Materials (ASTM). Standard test method for tensile properties of polymer matrix composite materials. ASTM D3039 / D3039M – 08, West Conshohocken, PA, USA, 2008.

[45] New Zealand Standard (NZS). Code of practice for general structural design and design loadings for buildings 1. NZS 4203: 1992, New Zealand.

[46] ACI Committee 440. Guide for the design and construction of externally bonded FRP systems for strengthening concrete structures. ACI 440.2R-17, American Concrete Institute, Detroit, MI, USA, 2017.

[47] T.H. Almusallam, H.M. Elsanadedy, Y.A. Al-Salloum, Effect of longitudinal steel ratio on behavior of RC beams strengthened with FRP composites – Experimental and FE study, J. Compos. Constr., ASCE 19 (1) (2015).

[48] S.T. Smith, J.G. Teng, FRP-strengthened RC beams, I: Review of debonding strength models, Eng. Struct. 24 (4) (2002) 385–395.

[49] M.A. Al-Saawani, A.K. El-Sayed, A.I. Al-Negheimish, Assessment of plate-end debonding design provisions for RC beams strengthened with FRP, Lat Am J Solids Struct 17 (2) (2020).

[50] R. Kalfat, R. Al-Mahaidi, S.T. Smith, Anchorage devices used to improve the performance of reinforced concrete beams retrofitted with FRP composites: State-of-the-art review, J. Compos. Constr., ASCE 17 (1) (2013) 14–33.

[51] S.V. Grelle, L.H. Sneed, Review of anchorage systems for externally-bonded FRP laminates, Int. J. Concr. Struct. M 7 (1) (2013) 17–33.

[52] H.A. Bengar, A.A. Shahmansouri, A new anchorage system for CFRP strips in externally strengthened RC continuous beams, J Build Eng 30 (2020) 101230.

[53] H.M. Elsanadedy, Y.A. Al-Salloum, T.H. Almusallam, Assessment of progressive collapse potential of special moment resisting RC frames – Experimental and FE study, Eng. Fail. Anal. 105 (2019) 896–918.

[54] T.B. Belytschko, C.S. Tsay, Explicit algorithms for non-linear dynamics of shells, J. Appl. Mech., Applied Mechanics Division, ASME 48 (1981) 209–231.

[55] Murray YD, Abu-Odeh A, Bligh R. Evaluation of concrete material model 159. Report No. FHWA-HRT-05-063, US Department of Transportation, Federal Highway Administration National Transportation Systems Center, USA, 2007.

[56] F.K. Chang, K.Y. Chang, A progressive damage model for laminated composites containing stress concentration, J. Compos. Mater. 21 (1987) 834–855.

[57] R.M. Christensen, A nonlinear theory of viscoelasticity for application to elastomers, J. Appl. Mech., Applied Mechanics Division, ASME 47 (1980) 762–768.

[58] H.M. Elsanadedy, T.H. Almusallam, S.H. Alsayed, Y.A. Al-Salloum, Flexural strengthening of RC beams using textile reinforced mortar – Experimental and numerical study, Compos. Struct. 97 (2013) 40–55.

[59] California Department of Transportation (Caltrans). Memo to designers 7-1 (Bridge Bearings). June 1994, 69p.

[60] J.F. Chen, J.G. Teng, Anchorage strength models for FRP and steel plates bonded to concrete, ASCE J. Struc. Eng. 127 (7) (2001) 784–791.

[61] X.Z. Lu, J.G. Teng, L.P. Ye, J.J. Jiang, Bond-slip models for sheets/plates bonded to concrete, Eng. Struc. 27 (6) (2005) 920–937.

[62] H.M. Elsanadedy, T.H. Almusallam, S.H. Alsayed, Y.A. Al-Salloum, Experimental and FE study on RC one-way slabs upgraded with FRP composites, KSCE J. Civ. Eng. 19 (4) (2015) 1024–1040.

[63] H.M. Elsanadedy, H. Abbas, Y.A. Al-Salloum, T.H. Almusallam, Prediction of intermediate crack debonding strain of externally bonded FRP laminates in RC beams and one-way slabs, J. Compos Constr, ASCE 18 (5) (2014).